Ore Geology Reviews 142 (2022) 104643

Contents lists available at ScienceDirect

Ore Geology Reviews

journal homepage: www.elsevier.com/locate/oregeorev

Towards the fertility trend: Unraveling the economic potential of igneous suites through whole-rock and zircon geochemistry (example from the Tapajós mineral Province, Northern Brazil)

Lucas Villela Cassini [a,b,*], Jean-François Moyen [c], Gabriel Cellier [a], Bruna de Freitas [a], Caetano Juliani [a], Oscar Laurent [d]

[a] Instituto de Geociências, Universidade de São Paulo, Rua do Lago 562, 05508-080 São Paulo, Brasil
[b] Mineração Caraíba S/A, Rua Jasmim do Serrado, 135, Tucumã, PA, Brasil
[c] Université de Lyon, Université Jean Monnet, UCBL, ENSL, CNRS, LGL-TPE, 23 rue Dr. Paul Michelon, F-42023 Saint Etienne, France
[d] Géosciences Environnemennt Toulouse - Observatoire Midi-Pyrénées, CNRS, 14 Av. Edouard Belin, 31400 Toulouse, France

ARTICLE INFO

Keywords:
Magmatic-hydrothermal deposits
Magmatic-arc
Amazonian craton
Tapajós
Gold
Copper
Geochemistry
Zircon

ABSTRACT

Magmatic hydrothermal mineral deposits axiomatically frame the hosting pluton and the given tectonic setting in which they are inserted. Unsurprisingly, pre-Cambrian porphyry deposits are different than Phanerozoic examples, as collisional or post-collisional deposits are different than arc-related mineralizing systems. As such, this contribution assesses the tectonic framework and the magmatic evolution of the igneous suites present in south-central Amazonian Craton (Tapajós Mineral Province, TMP), and how these parameters translate into metallogenetic potential for the formation of magmatic-hydrothermal copper and gold deposits. For this purpose we gathered whole-rock geochemistry data from selected TMP copper and gold deposits and present new in situ trace-element and U-Pb analyses in zircon grains.

The host rocks of the selected mineralizing systems belong either to the older magmatic sequence (OMS, 2.00–1.95 Ga), or to the younger magmatic sequence (YMS, 1.90–1.86 Ga). Whereas OMS presents characteristics of arc-related rocks, YMS represents the evolution towards post-orogenic or collisional setting. OMS might be divided into groups I, II and III granitoids. Group I comprises granites and granodiorites that mark the onset of the arc-magmatism in the TMP at ca. 2011 Ma. In this stage rocks are peraluminous, ferroan, anhydrous, show a strong crustal component and fO_2 values close to or below the fayalite-magnetite-quartz buffer (ΔFMQ), yielding metallogenetic unfertile pluton. These rocks correlate with the Cuiú-Cuiú Complex and comprise samples from the Patrocínio and Tocantinzinho deposits. Group II granitoids correlate with the Creporizão Suite and comprise Tocantinzinho, São Jorge, Chapéu do Sol and Patrocínio deposit samples (with extrusive equivalents in the Coringa deposit). Rocks are metaluminous to peraluminous, magnesian to ferroan and mark the evolution of the magmatism towards more oxidizing ($0 \leq \Delta FMQ \leq +4$), hydrous and metallogenetically fertile conditions at ca. 1986 Ma. Mineralized zones are defined by gold bearing sulfide veins and veinlets within the potassic or sericitic alteration halos. Group III comprises rarer high-K, metaluminous, ferroan, anhydrous and reduced syenites and monzonites dated at 1993 and 1974 Ma, generated by decompression melting of metasomatized mantle. By itself, group III rocks should be considered as unfertile batches of magma, however, its interaction with the coeval, more hydrous and oxidized group II melts, confer these magmas their metallogenetic potential. Mineralization in group III rocks is defined by disseminated pyrrhotite – pyrite ± gold within the sericitic, chloritic and/or carbonate alteration zones.

YMS comprises intermediate and acid rocks that belong to the Parauari Intrusive Suite and to the Iriri Group. Whereas, intermediate volcanics from YMS evolved on a hydrous and reduced petrologic trend, acid volcanics and the Batalha and Palito granitoids evolved on a dry and reduced trend, reflecting a change on TMP's tectonic context, from magmatic-arc to a post-orogenic or collisional tectonic setting. Despite the reduced and anhydrous characteristic of the magmas, YMS's metallogenetic potential is related with remobilization or melting of SCLM or lower crustal Au-rich sulfides formed on the previous magmatic events. Hence, the first pulses of the YMS might be considered as potentially fertile for the formation of Au-rich magmatic-hydrothermal deposits.

* Corresponding author. Permanent address: Rua Iquiririm, 28, Vila Indiana, CEP: 05586-000, São Paulo, SP, Brasil.

https://doi.org/10.1016/j.oregeorev.2021.104643
Received 15 March 2021; Received in revised form 2 August 2021; Accepted 8 December 2021
Available online 3 January 2022

1. Introduction

The metallogenic process requires the presence of fertile rocks that provide not only metals but also ligands, fluids and the volatile contents necessary to form an anomalous concentration and define a mineral deposit. Magmatic-hydrothermal mineral systems, particularly the copper and gold porphyry-epithermal class, are genetically connected with oxidized ($\Delta FMQ > 0$), hydrous (2–6 wt% H_2O), subduction-related, intermediate to acid igneous suites, intruded at shallow depths (Cooke et al., 2014; Loucks, 2014; Pirajno, 2009; Richards, 2015a, 2011a; Sillitoe, 2010; Sinclair, 2007; Sun et al., 2015). Despite the occurrence of porphyry deposits at collisional and at extensional settings (Chen et al., 2015; Richards, 2015b, 2014, 2009; Wang et al., 2018), it is unquestionable that these deposits occur preferentially at destructive plate margins. Therefore, at a given geologic context, it is important in terms of prospective criteria, to identify which igneous suites are directly related with the magmatic-arc. This separation is straightforward in Phanerozoic subduction zones such as seen in the Andean Cordillera or in the west Pacific rim. The problem arises when we look at ancient and cratonized terrains, where the arc-related sequence appears juxtaposed with the collisional, post-collisional and anorogenic units. A first order problem in this case, is that not all arc-magmas are prone to form magmatic-hydrothermal mineral deposits, even though the reason, processes and features that render a given magmatic system fertile or not

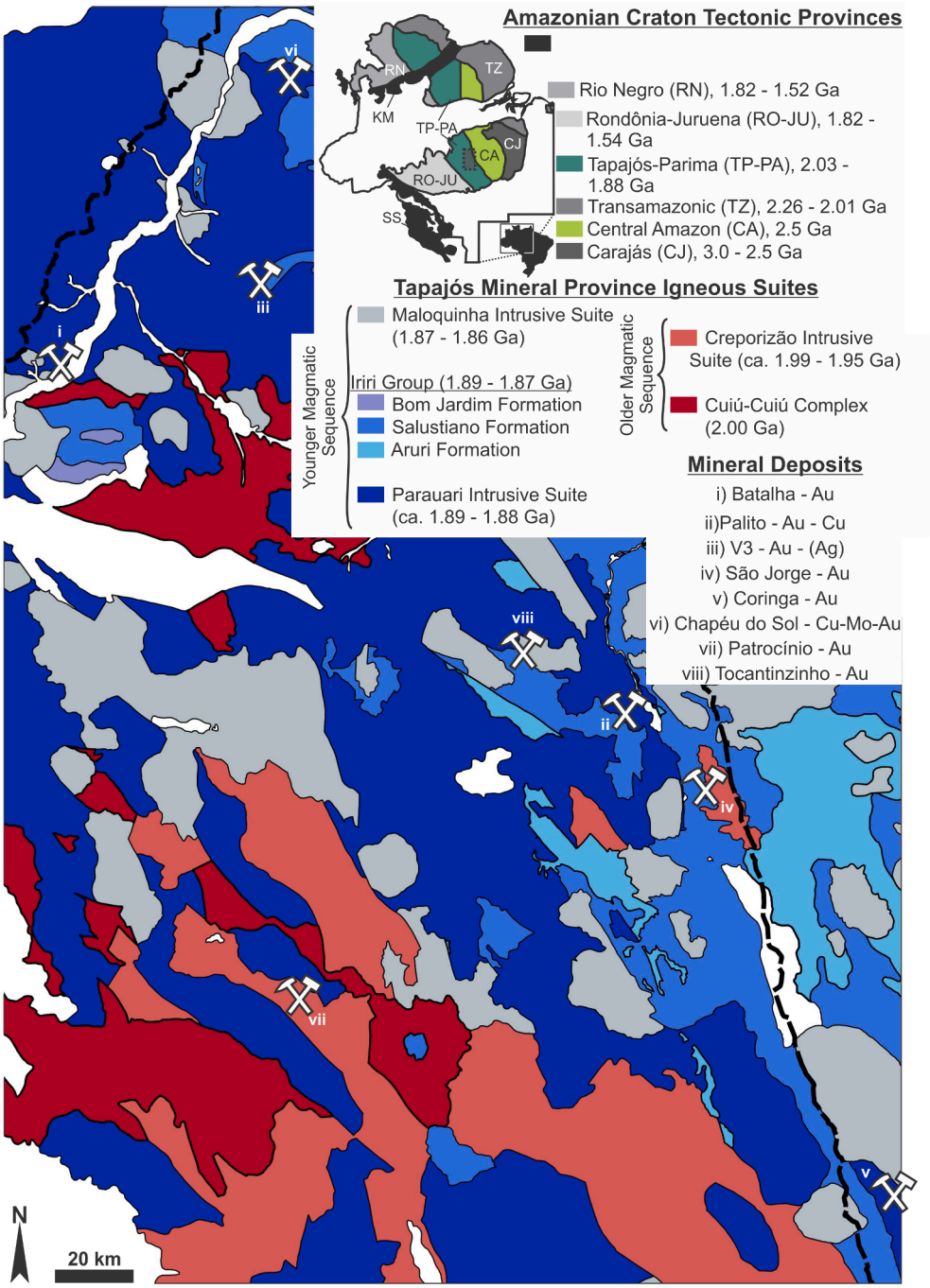

Fig. 1. Amazonian Craton and its tectonic subdivision (Santos et al., 2006; Santos et al., 2000). The Tapajós Mineral Province (TMP) geologic map, adapted from Klein et al. (2001), brings the main Orosirian igneous suites and the selected mineral deposits involved in this contribution. Mafic bodies and Phanerozoic units are not colored. Main roads are marked by the black dashed lines.

are still unclear (e.g., Zhang and Audétat, 2017). The physiology of ancient subduction-zones is not particularly helpful and characteristics such as the absence or diffuse suture zone and ambiguous geochemical signature due to metamorphism and/or weathering are common caveats. Additionally, whereas fluid-flux mantle melting is easily achieved in modern subduction zones, yielding hydrous and metallogenetic fertile magmas, the tectonic and petrogenetic mechanisms behind Paleoproterozoic (or older) rocks are still dubious. Despite these peculiarities, the Archean Spinifex Ridge (Mo – Cu) located at eastern Pilbara Craton (Huston et al., 2007) and the Paleoproterozoic Malanjkhand deposit (Cu – Mo – Au) at central India (Stein et al., 2004) are good examples of high-tonnage Precambrian porphyry deposits.

Within this topic, the south-central portion of the Amazonian Craton, a region known as Tapajós Mineral Province (TMP) consists on a promising area (Fig. 1). It comprises arc-related, collisional and post-collisional igneous suites, that distribute within the 2.0–1.86 Ga age interval and host gold (copper and molybdenum in a lesser extent) mineral deposits (Borgo et al., 2017; Juliani et al., 2005; Lamarão et al., 2002; Santos et al., 2004; Santos et al., 2001). Most recent papers describe TMP's mineralizations as porphyry-epithermal mineral systems (e.g. Cassini, 2016; Echeverri Misas, 2015; Juliani et al., 2005; Lopes and Moura, 2019; Tokashiki, 2015), yet, Intrusion-Related-Gold-Systems (IRGS) (Santos et al., 2001; Villas et al., 2013) and hybrid porphyry-IRGS models have also been proposed (Biondi et al., 2018; Borges et al., 2009; Juliani et al., 2002). Despite the effort over the past years, there are still important knowledge gaps that need to be filled so we can constrain the TMP's true economic potential.

Ergo, the central point of this study is to investigate how the host rocks of different mineral deposits at the TMP evolved, examine their general geochemistry characteristics, pinpoint the main differences and similarities and elucidate how and why these magmas became fertile. The data approach given by Loucks (2014), for example, where the author constrains the fertility of plutons by looking at their geochemical signature (i.e. copper-producing plutons show higher whole-rock Sr/Y and V/Sc ratios, used as proxies to the hydrous condition of the magmas) is rather pertinent for our purpose. In this regard, we gathered information and organized a geochemistry database for selected Au – Cu – Mo mineral deposits and occurrences identified in the TMP. In addition, we provide new U-Pb and trace-element analyses in zircon grains from samples collected at central TMP to assess the magmatic evolution of the intrusions. Zircon Ce contents is used to estimate the oxygen fugacity of the rocks and consequently their metallogenetic potential (i.e. typical porphyry deposits are genetically related with plutons with fO_2 greater than the fayalite-magnetite-quartz oxygen buffer (Richards, 2015a)). Ultimately, by combining both empirical and theoretical approaches, our purpose is to establish a prospective criteria and a systematic capable of constraining the metallogenetic potential of different igneous suites not only from the TMP, but also from other cratonic terrains.

2. Geologic framework of the Tapajós mineral Province

The Tapajós Mineral Province (TMP) is part of the south-central Amazonian Craton (AC), on the limit between the Ventuari-Tapajós or Tapajós-Parima and Central Amazonian tectonic provinces (Santos et al., 2000; Tassinari and Macambira, 1999). According to Santos' tectonic model (Fig. 1), the Tapajós-Parima Province is the result of a Paleoproterozoic collisional-orogen that, among other consequences, was responsible for the expressive orogenic and post-orogenic magmatism that predominates in the region. This model has been revisited by many authors over the past years. More recently, Carneiro et al. (2019), supported by high-resolution magnetometry data, claim that the magmatic-arc sequence was built on Archean basement, previously restricted to the Central Amazonian and Carajás Provinces. According to the authors, NNW-SSE lineaments that agrees with Santos' model are intrinsically related with the shallower crustal levels, whereas deeper (>15 km) E-W trending lineaments are related with the Archean basement, which led the authors to suggest an alternative crustal framework for this part of the AC.

2.1. Lithostratigraphy

In general, the older units described at the TMP represent different stages of the arc magmatism, whereas the tectonic affinity of the younger sequence remains less consensual (Table 1 presents a summary of TMP's lithostratigraphic units). The igneous suites within the 2.0 – 1.95 Ga age interval, addressed hereafter as the older magmatic sequence (OMS), encompasses: the Cuiú-Cuiú Complex (tonalites and granodiorites of ca. 2.04–1.99 Ga); the Vila Riozinho Formation (basaltic-andesite, trachyte, rhyolite of 2.0 Ga); and the Creporizão Intrusive Suite (granitoids of ca. 1.98–1.95 Ga, ages after Lamarão et al. 2002; Santos et al., 2004; Santos et al., 2001; Santos et al., 2000).

Approximately 50 million years separate the OMS from the younger magmatic sequence (hereafter YMS). The Tropas and Parauari Intrusive Suites (1.90–1.87 Ga) mark the onset of the younger magmatism, characterized by tonalite and granodiorites, with syeno-, monzogranites and acid volcanics for the later. These are followed by the volcanic rocks of the Iriri Group and its subdivisions, accordingly: Bom Jardim Formation (intermediate to acid volcanics with subordinate ignimbrites of 1.89–1.88 Ga); Salustiano and Aruri Formations (rhyolites, ignimbrites of dacitic composition and volcanic breccias of 1.88–1.87 Ga); and Moraes Almeida Formation (rhyolites and trachytes of ca. 1.88 Ga, ages and descriptions after Dall'Agnol et al., 1999; Juliani et al., 2005; Lamarão et al., 2002; Santos et al., 2000)). Often, YMS volcanics define dykes or lava flows covering OMS plutons. The Maloquinha Intrusive Suite represents the last stage of YMS and comprises syeno- and alkali-feldspar granites of ca. 1.87 Ga (Lamarão et al., 2002; Santos et al., 2002) that define round shaped plutons.

2.2. Typology and general features of the mineralizing systems at the TMP

The results presented in this contribution refer to selected mineral deposits chosen in order to cover most part of the TMP. Accordingly, the Batalha, V3 and Chapéu do Sol gold deposits are found in northern TMP; central TMP is represented by the Tocantinzinho, Palito and São Jorge gold mineralizations; and the Patrocínio and Coringa gold deposits are found in southern TMP. The Patrocínio, Tocantinzinho and Coringa deposits are hosted by the OMS, the first two by ca. 1.97 Ga granitoids that correlate with the Creporizão Intrusive Suite, and the latter is found within coeval volcanics. The Batalha, Palito and V3 deposits are hosted by YMS granitoids and volcanic breccias (the case for the later), whereas the São Jorge and Chapéu do Sol deposits are uniquely associated with both magmatic sequences (Echeverri Misas, 2015; Lamarão et al., 2002). Table 2 summarizes the main features of the mineral deposits selected at this study.

2.2.1. Deposits within the older magmatic sequence (OMS)

The Patrocínio gold mineralization (southern TMP) is found in strongly hydrothermalized (K-metasomatism and sericitic alteration), calc-alkalic, metaluminous to peraluminous, syeno- and monzogranites of ca. 1.97 Ga (Fig. 2a–i), into which gold bearing sulfide veins and veinlets are injected (Cassini, 2016). A disseminated type of mineralization was also identified and is associated with syenites and monzonites (Fig. 2j–m) affected by sericitic, chloritic and carbonate hydrothermal alterations, where the mineralization is characterized by the assemblage pyrrhotite-pyrite ± gold, with traces of chalcopyrite. On the distal zones, barren propylitic alteration was identified and commonly overprints the potassic and sericitic alterations. Even though the Patrocínio mineralization has many attributes of porphyry systems, the magmatic-hydrothermal system still requires additional efforts for a better understanding and a more detailed comprehension.

The Tocantinzinho gold deposit (central TMP), the largest at the TMP with 1.7 million oz. of gold (Borgo et al. 2017), presents a similar

Table 1
Summary of the main igneous suites that encompasses TMP's older and younger magmatic sequences (modified from Cassini et al., 2020).

Lithostratigraphic Unit		Description	Geotectonic Context (references between brackets)	Hosted mineral deposits (*)
Younger Magmatic Sequence (YMS)	Iriri Group 1.89–1.87 Ga [2]	• Rhyolite and trachyte • Tuff, ignimbrite and volcanic breccia • Rhyolite and ignimbrite • Andesite, dacite, trachyandesite, latite, rhyolite and ignimbrite	• Post-collisional/anorogenic (5;6) • Magmatic-arc/post-orogenic (4) • Magmatic-arc (4) • Magmatic-arc (4)	V3 (Au); Chapéu do Sol (Cu-Mo-Au)**
	Parauari Intrusive Suite 1.89–1.87 Ga [2;3;6]	Biotite-hornblende monzo- and syenogranite, tonalite, granodiorite	Magmatic-arc (2;3); Post-collisional (6)	Batalha (Au); Palito (Au-Cu)
Older Magmatic Sequence (OMS)	Tropas Suite 1.90–1.88 Ga [2]	Tonalite and granodiorites	Island-arc (2;3)	–
	Creporizão Intrusive Suite 1.98–1.95 Ga [2;3]	Monzo-, syenogranite, granodiorite and tonalite	Magmatic-arc (2;3)	Patrocínio (Au); Tocantinzinho (Au)
	Vila Riozinho Formation 2.00 Ga [5]	Basaltic-andesite, trachyte, rhyolite	Magmatic-arc (5)	Coringa
	Cuiú-Cuiú Complex 2.04–1.99 Ga [1;2]	Gneiss, migmatite, granitoids, amphibolite	Island-arc (1;2;3); Magmatic-arc (6)	–

(*) The São Jorge and Coringa deposits haven't been correlated with any TMP lithostratigraphic unit; **The Chapéu do Sol deposit is associated with both older and younger magmatic sequences. (1) Santos et al. (2000); (2) Santos et al. (2001); (3) Santos et al. (2004); (4) Juliani et al. (2005); (5) Lamarão et al. (2002); (6) Juliani et al. (2002); (7) Guimarães et al. (2021).

Table 2
Host rocks, mineralizing style and hydrothermal alteration evolution of the selected TMP mineral deposits.

Deposit/Mineral occurrence	Host Rocks	Mineralization Style	Hydrothermal Alteration						References
			Sodic	Potassic	Propylitic	Sericitic	Argilic	Adv. Argilic	
V3 (Au)	1.89–1.87 Ga volcanic rocks (Iriri Group)	Hydrothermal breccias and veins	Pl	Kfs, Amp, Bt, Qz, ±Hm ± Sul	Pl, Kfs, Qz, Ser, Chl, Ep, Cab ± Amp ± Sul	Qz, Dk, Ser, Chl, ±Alu ± Sul	Dk, Kao, Ser, Chl, ±Pl ± Kfs	Pyr, Alu, Dsp, Rt, And, Sul, Cu, Ag, Au, ±Hm ± Dk ± Kao	Echeverri Misas (2015)
Palito (Au - Cu)	1.88 Ga granitoids	Veins and disseminated	Pl, Bt, ±Kfs ± Amp ± Qz	Kfs, Qz, ±Pl ± Amp ± Bt ± Hm	Pl, Ser, Chl, Ep, Ttn, Cab ± Sul	Pl, Kfs, Qz, Ser, Sul ± Au ± Cu	Pyr, Kao, Ser, Sul ± Pl ± Kfs	–	Echeverri Misas (2015)
Batalha (Au)	1.88 Ga granitoids	Veins and disseminated	Pl	Kfs, Bt, Qz	Pl, Chl, Ep, Cab, Sul, ±Qz ± Au	Qz, Ser, Sul, Au, Fl ± Cab	–	–	Juliani et al. (2002)
São Jorge (Au)	OMS and YMS granites	Veins and disseminated	Qz, Pl, Kfs, Bt, Ttn, Mag		Pl, Bt, Chl, ±Ep ± Cab ± Ser ± Sul ± Mag ± Qz ± Kfs	Qz, Cab, Sul, Ser ± Pl ± Kfs ± Bt	–	–	Lamarão et al. (2002); Borges et al. (2009)
Chapéu do Sol (Cu - Mo - Au)	OMS and YMS volcanics and subvolcanics	Disseminated, veins and veinlets	Pl	Pl, Bt, Kfs, Qz	Pl, Qz, Chl, Ep, Rt, Ttn, Sul, Cab, ±Hm ± Amp	Qz, Ser, Adu, Sul, Au, ±Ttn ± Cab ± Bt	Qz, ill, Kao ± Hm	–	Echeverri Misas (2015)
Patrocínio (Au)	1.99–1.95 Ga granites, syenites and monzonites	Veins and veinlets ± disseminated	Pl	Kfs, Qz	Chl, Ep, sodic-Pl	Ser, Py, Po, ±Au	Chl, ±Ccp	–	Cassini (2016)
Tocantinzinho (Au)	1.98 Ga granites	Disseminated and veinlets	–	Kfs, Qz, Pl, Ep, Chl, Py, Ccp, Au ± Hm		Ser, Py, Au, Qz, Ccp, Gn, Sp, ±Hm ± Pl	–	–	Borgo et al. (2017); Lopes and Moura (2019); Biondi et al. (2018)
Coringa (Au)	1.97 rhyolites	Veins and veinlets	–	Kfs, Bt, ±Qz	Chl, Ep, Qz, Pl, ±Cab ± Py	Qz, Ser, Ccp, Sp, Gn, ±Adu	ill	–	Tokashiki (2015) Guimarães et al. (2021)

Adu: adularia; Alu: alunite; Amp: amphibole; And: andalusite; Bt: biotite; Cab: carbonate; Ccp: chalcopyrite; Chl: chlorite; Dk: dickite; Dsp: diaspore; Ep: epidote; Fl: fluorite; Gn: galena; Hm: hematite; ill: illite; Kao: kaolinite; Kfs: K-feldspar; Mag: magnetite; Pl: plagioclase; Po: pyrrhotite; Py: pyrite; Qz: quartz; Rt: rutile; Ser: sericite; Sp: sphalerite; Sul: sulfide; Ttn: Titanite.

geologic framework. It is hosted by metaluminous to peraluminous monzogranites, granitic breccias, aplite and pegmatites of ca. 1.98 Ga, that are affected by an early stage of K-metasomatism, followed by sericitic, chloritic and carbonatic alterations (Biondi et al., 2018; Lopes and Moura, 2019). In this context the mineralization is intimately related with the sericitic alteration and is represented by disseminated gold or quartz-sulfide, gold bearing veinlets. The most common sulfide is pyrite, however, late forming chalcopyrite, sphalerite and galena have also been reported. Biondi et al. (2018) claim that the Tocantinzinho's magmatic-hydrothermal system shows features that resemble both intrusion-related-gold-systems (IRGS) and gold-rich porphyry deposits. Lopes and Moura (2019), on the other hand, are more emphatic and describe the deposit as a "porphyry-style" mineralization since it lacks typical features of Phanerozoic (*stricto sensu)* porphyries.

The Coringa deposit (southern TMP) is hosted by volcanic rocks of ca. 1.97 Ga (Fig. 2n), with minor intrusive bodies that are coeval with the Creporizão Intrusive Suite. According to Guimarães et al. (2021) and Tokashiki (2015) the volcanic units are dominantly rhyolites and the volcanoclastic sequence is represented by volcanic-breccias, lithic-, lapilli- and crystal-tuffs, with subordinated ignimbrites. The mineralization is hosted by sericitic altered rhyolites and alkali feldspar granites, that define topographic domes, and is focused on brittle structures

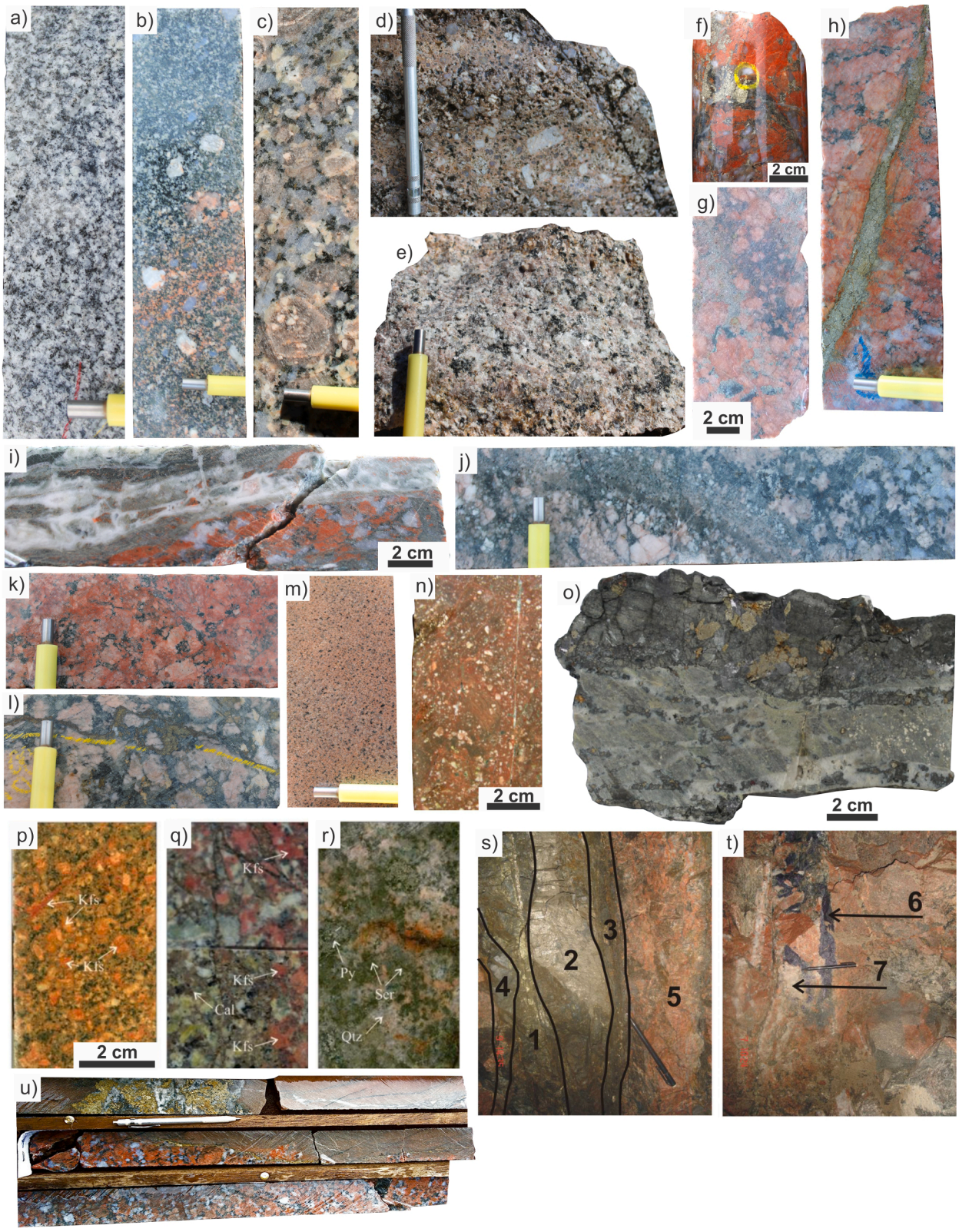

(caption on next page)

Fig. 2. Typology of the different OMS (a – o) and YMS rocks (p – u). (a) Massive, leucocratic, granodiorite drill core sample. (b) Massive, partially altered (potassic alteration), granodioritic porphyry; (c) Porphyritic and massive syenogranite with compositionally zoned plagioclase phenocrysts; (d) Syenogranitic porphyry with plagioclase phenocrysts (outcrop near the Patrocínio area); (e) Equigranular, massive monzogranite; (f) Strongly altered (potassic alteration) granite, with gold bearing pyrite in chlorite-sericite veinlets; (g) Sulfide bearing, chlorite-sericite alteration in K-metasomatized granitoid; (h) Gold bearing, quartz sulfide vein injected near the granite-syenite contact. Rocks have previously experienced pervasive potassic and subsequent chlorite-sericite alteration; (i) Granite drill-core sample with multi-phasic hydrothermal events. early potassic alteration (reddish feldspar crysts) is followed by fissural and interstitial chlorite-sericite alteration (gray-greenish color). The last hydrothermal event is represented by the white-silica infilled breccia; (j) Drill core sample with contact between monzonite (left) and monzogranite (right) with a reaction rim (central) and small opaque (sulfide?) crysts; (k) Potassic and chlorite-sericite altered syenite; (l) Chlorite-sericite and potassic altered monzonite with disseminated, gold bearing sulfide (pyrite and pyrrhotite), and less frequent sulfide veinlets; (m) Aplitic syenite found as synplutonic dykes in OMS granites. (n) Rhyolite with feldspar phenocrysts and potassic alteration form the Coringa deposit; (o) Coringa deposit ore example, with strongly sericitic altered volcanic rock (rhyolite?) cross-cut by a chalcopyrite + sphalerite + galena vein, brecciated by sericitic + white silica alteration. (p – t) Palito deposit samples (examples from Echeverri-Misas, 2015; (p) potassic altered granite with secondary K-feldspar; (q) potassic and propylitic alteration with K-feldspar, chlorite, epidote and carbonate (Cal); (r) Sericitic alteration with quartz (Qtz), sericite (Ser) and pyrite (Py); (s) Sulfide vein in strongly hydrothermalized granite (5), with (1) chalcopyrite, (2) pyrite, (3) breccia zone and (4) quartz veins; (t) Strongly hydrothermalized granite with fluorite (6) and white silica veining (7). (u) OMS granite injected by YMS dacite dyke with white silica, gold bearing sulfide pocket and smaller veinlets along the dyke contact.

represented by quartz bearing veins and veinlets with galena, pyrite, chalcopyrite and gold (Fig. 2o). Guimarães et al. (2021) and Tokashiki (2015) described the Coringa deposit as an intermediate-sulfidation due the presence of adularia and Mn-carbonates on the mineralized veins. However, Tokashiki (2015) believes that the deposit was initially a low sulfidation system that evolved to intermediate sulfidation conditions, without discarding the potential of a deeper and genetically connected porphyry system. Measured and indicated reserves sum a total of 516.000 oz. of gold (Tokashiki, 2015).

The Chapéu do Sol (copper, molybdenum and gold) mineralization (northern TMP) is genetically related with volcanic and volcanoclastic sequences, with coeval porphyry and granitic stocks, formed in two age intervals: one at 1.99 – 1.97 Ga and a 100 Ma younger one, at 1.88 – 1.86 Ga (Echeverri Misas, 2015). The high-K affinity of the igneous suites led the author to suggest a mature arc tectonic context. The mineralization is represented by disseminated sulfide (pyrite, chalcopyrite, molybdenite and sphalerite), or gold bearing sulfide veins and veinlets, more frequently found on the sericitic alteration halos with adularia. Echeverri Misas (2015) describes the Chapéu do Sol mineralization as a low-sulfidation system.

2.2.2. *Deposits within the younger magmatic sequence (YMS)*

Among the deposits hosted by the YMS, the Batalha, Palito and São Jorge are hosted by biotite and amphibole bearing syeno- and monzogranites, whereas the V3 is hosted by intermediate to acid volcanic rocks.

The Batalha gold deposit (northern TMP) is a magmatic-hydrothermal system hosted by granitoids of 1.88 Ga that correlate with the Parauari Intrusive Suite (Juliani et al., 2002). The hydrothermal system is characterized by early Na-metasomatism, followed by potassic, propylitic and late sericitic alterations (the latter two the most important for the mineralization). Within the propylitic zone, ore consists in disseminated pyrite with gold inclusions, or gold bearing quartz veins with carbonate, fluorite, pyrite, chalcopyrite and chlorite. On the sericitic zone, gold mineralization is found either on fissures or in pervasive style with quartz, sericite, pyrite, chalcopyrite and galena. As proposed by Juliani et al. (2002) the Batalha hydrothermal system is compatible with a porphyry Au-Cu deposit, with some features of IRGS.

The Palito gold and copper deposit (central TMP) is hosted by ca. 1.88 Ga granitoids that according to Echeverri Misas (2015) correlates with the late stages of the Parauari Intrusive Suite, on a collisional or post-collisional tectonic setting. It presents potassic, propylitic and sericitic hydrothermal alteration zones and mineralization consists mainly on sulfide bearing, NW-SE and E-W trending quartz veins and veinlets within the sericitic alteration halo, with less frequent disseminated sulfides (Fig. 2p–t). Chalcopyrite is the main sulfide associated with the gold mineralization, but pyrite, galena, pyrrhotite and Bi bearing minerals were also identified. Echeverri Misas (2015) describes this magmatic-hydrothermal system as a porphyry Au-(Cu) deposit.

The São Jorge gold deposit (central TMP) is hosted by the homonymous granite that was divided by Lamarão et al. (2002) on the older and younger São Jorge granites (1.98 and 1.89 Ga respectively), the latter more closely related with the mineralization. Similarly to the Batalha deposit, it shows mineralization focused on the propylitic and sericitic alteration halos, where gold is usually associated with pyrite veins and veinlets. A disseminated type of mineralization is also identified but is comparatively rarer. Other than pyrite chalcopyrite, sphalerite, molybdenite and galena were also described (Borges et al., 2009; Lamarão et al., 2002). Borges et al. (2009) claim that the deposit has geological attributes of both IRGS and porphyry systems.

Differently than the other YMS hosted deposits, the V3 gold mineralization (northern TMP) is associated with hydrothermal breccias developed on the volcanic and volcanoclastic sequence of the Iriri Group (1.89–1.87 Ga), with coeval shallow level granitic stocks. The hydrothermal system comprises pervasive and fissural potassic, silicic, propylitic, sericitic, argilic and advanced argilic alunite bearing alterations. The latter hosts the highest gold contents, however, the potassic, propylitic and sericitic alteration zones also show considerable sulfide contents. $^{40}Ar/^{39}Ar$ dating in alunite crystals acquired by Echeverri Misas (2015) yielded 1.86–1.84 Ga, which is interpreted as the age of mineralization. The author describes the deposit as a high-sulfidation epithermal system.

In fact, YMS volcanic rocks are often found as dykes in OMS granitoids (the association has been reported in the Tocantinzinho, Patrocínio and Palito deposits) and potentially define an additional type of mineralization, characterize by gold bearing pyrite veins and veinlets injected along the contact between the intrusive and subvolcanic units (Fig. 2u).

3. Methods

The results presented in this contribution refer to whole-rock and zircon geochemistry/isotopic analyses. The whole-rock geochemistry database counts with published and unpublished results from selected deposits in order to cover most part of the TMP, and involves results from Biondi et al. (2018), Cassini (2016), Echeverri Misas (2015), Gutiérrez (2018), Juliani et al. (2002), Lamarão et al. (2002), Lopes and Moura (2019) and Tokashiki (2015) (geochemistry database is available as supplementary material). In-situ measurements of trace-elements in zircon grains were performed in OMS samples collected in central TMP. Three new U-Pb dating results are presented coupled with two reexamined analyses published by Cassini et al (2020).

Whole-rock geochemistry data was treated with GCDKit (Janoušek et al., 2006) and modelling routines of fractional crystallization were performed using further R programming (Janoušek et al., 2016). Major elements were modeled through simple mass-balance and trace-elements through Rayleigh crystallization using partition coefficients from Rollinson (1993) and GERM database (available at http://earthref.org).

Trace-elements and U-Pb geochronology analyses in zircon grains

were performed at the Department of Earth Sciences (ETH - Zürich) using a Thermo Element XR, sector field, single collector ICP-MS coupled to a 193-nm Resolution S155 (ASI) laser ablation system. The later counts with a two-volume Laurin Technic ablation cell fluxed by high-purity He at 0.5 l min^{-1} rate. The 20 μm spots were ablated for 30 s with a repetition rate of 3 Hz and a laser energy of 2 J cm^{-2}. Ar was admixed to the aerossol within the ablation funnel (0.96 l min^{-1}) to carry the ablated material for ionization. The integration time per point was 0.662 s, and elemental concentration was calculated using the software Iolite (Paton et al., 2011). The stoichiometric Si content of zircon (15.2 wt%) was used as internal standard for trace element quantification and U-Pb data reproducibility was assured by analyses of reference zircon grains (AUSZ7-1, OG-1, Plešovice and 91500). U-Pb and trace element measurements were acquired at the same spot, and fractured or metamict domains were avoided. Zircon trace element results were treated with GCDKit and U-Pb data with IsoplotR (Vermeesch, 2018), results are also available as supplementary material.

We use the $X^{melt}_{Ce^{4+}}/X^{melt}_{Ce^{3+}}$ index (Smythe and Brenan, 2016), to constrain the fO_2 of the magmas from central TMP (equations 1 and 2). Most zircon based oxy-barometers available in the bibliography (Ballard et al., 2002; Chelle-Michou et al., 2014; Smythe and Brenan, 2016; Trail et al., 2012) rely on the lattice strain model (Blundy and Wood, 1994) and are strongly influenced by the LREE content of zircon. The lattice strain model satisfactorily explains the behavior and HREE, but LREE, on the other hand, commonly deviates from the model predictions, compromising the robustness of most oxy-barometers. As demonstrated by Zou et al. (2019), Smythe and Brenan's $X^{melt}_{Ce^{4+}}/X^{melt}_{Ce^{3+}}$ index might be considered as REE independent and magmatic fO_2 is estimated with basis on the temperature of the magmas (Ti-in-zircon thermometer from Ferry and Watson (2007), assuming SiO_2 and TiO_2 activities of 1.0 and 0.65 respectively), non-bridging oxygens (NBO, Virgo et al., 1980) and mole fraction of water (estimated with the hygrometer from Waters and Lange, 2015) as it follows:

$$1)\ \frac{X^{melt}_{Ce^{4+}}}{X^{melt}_{Ce^{3+}}} = \left[\frac{\sum Ce_{zircon} - \left(\sum Ce_{melt} * D^{zircon/melt}_{Ce^{3+}}\right)}{\left(\sum Ce_{melt} * D^{zircon/melt}_{Ce^{4+}}\right) - \sum Ce_{zircon}}\right] * 1.04877;$$

$$2)\ ln\left[\frac{X^{melt}_{Ce^{4+}}}{X^{melt}_{Ce^{3+}}}\right] = \frac{1}{4}\ln fO_2 + \frac{13136(\pm 591)}{T} - 2.064(\pm 0.011).$$

$$\frac{NBO}{T} - 8.878(\pm 0.112).xH_2O - 8.955(\pm 0.091)$$

4. Results

4.1. Whole-Rock geochemistry

In this section we directly compare whole-rock geochemistry analyses from the different TMP deposits. As a first selection criteria and in view of the thick weathering profile at the Amazonian region, the whole-rock geochemical data were plotted on the MFW diagram after Ohta and Arai (2007) (Fig. 3). The diagram was idealized with basis on a dataset of igneous rocks and their respective weathered products, where principal component analysis allows the M and F vertices to capture mafic to felsic differentiation sequence, whereas the W apex relates with the degree of weathering. Accordingly, the samples that plot on the center of the diagram and scatter towards the W vertice likely present some degree of weathering that might disturb their original geochemical signature and, consequently, these samples were excluded from the database.

4.1.1. Classification diagrams

With respect to their geochemical classification, the most prominent

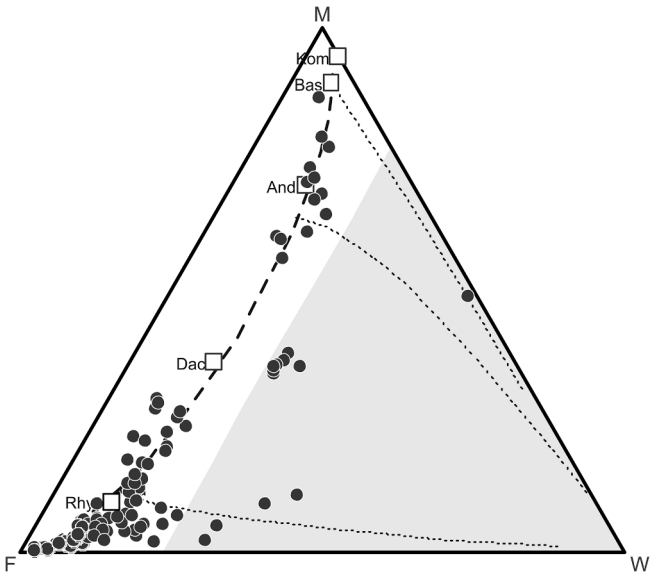

Fig. 3. FMW ternary diagram after Ohta and Arai (2007) for the whole-rock geochemistry database. Samples that plot on the shaded area indicate higher degree of weathering and were not considered for the results and discussion sections.

difference between the older and younger igneous suites is the much wider compositional range covered by the former, in particular for the intrusive sequence (Fig. 4a). The Tocantinzinho, São Jorge and Patrocínio deposit rocks show a significant variation on the diagram and vary between diorites, monzonites, quartz-monzonite, granodiorites, tonalites and granites. The later also shows lower silica syenites, quartz-syenites and syeno-diorites. The Chapéu do Sol rocks show a smaller variation and plot on the quartz-syenite, granite and alkali-granite fields. Equivalent compositions are verified for the Coringa deposit, with the extrusive sequence essentially rhyolitic or alkali-rhyolitic.

The intrusive sequence of YMS (Palito, São Jorge and Batalha deposits) shows a much narrower geochemical variation (Fig. 4b). The three deposits host rocks vary between granite and alkali-granite with a single granodiorite sample for the Batallha deposit. The V3 deposit is hosted by a volcanic sequence that is dominated by rhyolites, dacites, lati-andesites and, more rarely, quartz-trachyte.

The diagrams from Fig. 5 brings SiO_2 vs. Fe-index, SiO_2 vs. MALI and an A-B plot for constraining the sample's aluminosity (Frost et al., 2001; Villaseca et al., 1998). In this study we gave preference to use Villaseca's A-B diagram instead of the classic A/CNK vs. A/NK plot (Shand, 1943). The former brings aluminosity as a function of maficity, hence petrologic trends are more promptly identified. In general, the OMS deposits are magnesian to slightly ferroan (Fig. 5a), calc-akalic to alkali-calcic (Fig. 5b) and metaluminous to moderately peraluminous, defining a negative slope on the A-B plot (Fig. 5c). This general trend accounts for the Tocantinzinho, São Jorge and Chapéu do Sol deposits, the latter with a few alkalic samples. The Patrocínio and Coringa samples behave differently and tend to plot on the magnesian-ferroan transition or are fully ferroan granitoids (the case for lower silica Patrocínio samples), vary from calc-alkalic to alkalic and are metaluminous to felsic-peraluminous.

Within the YMS, the Palito and Batalha samples are ferroan, alkali-calcic and metaluminous to moderately-peraluminous. On the A-B diagram, the Batalha granitoids do not define any noticeable trend and instead, samples cluster around the same value of maficity (at approximately B = 40) and spread towards the low-peraluminous and moderately-peraluminous fields. The V3 volcanics resemble the trend identified for the OMS, with magnesian intermediate samples and ferroan acid members that vary from alkalic to calc-alkalic and define a

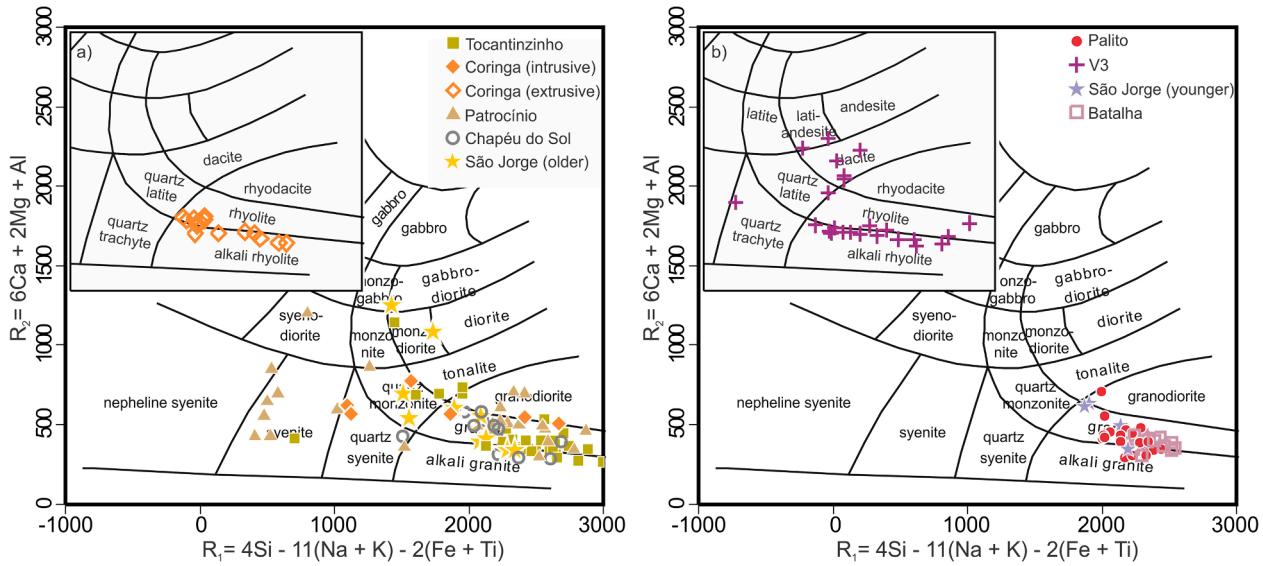

Fig. 4. De la Roche et al. (1980) classification diagram for the OMS (a), with coeval volcanics from the Coringa deposit at the top-left. (b) Classification diagram for the YMS with the V3 volcanics plotted at the smaller top-left diagram.

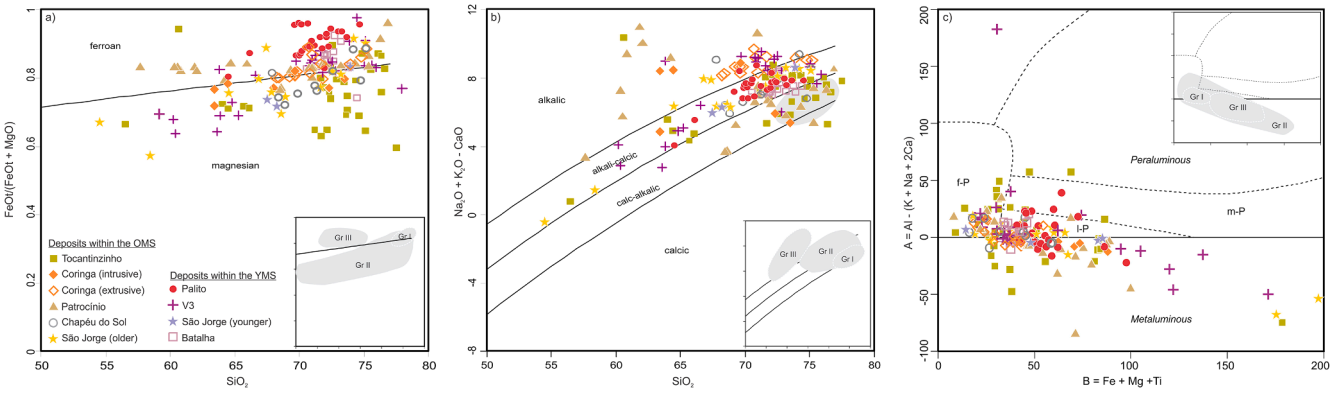

Fig. 5. Frost's classification diagrams for OMS and YMS, with SiO_2 vs. Fe-index (a), SiO_2 vs. MALI (b), and A-B diagram after Villaseca et al. (1998) (c), where A = Al - (K + Na + 2Ca) and B = Fe + Mg + Ti, calculated for millications. Extrusive rocks from the Coringa and V3 deposits are plotted for comparison purposes.

clear negative slope on the A-B diagram from metaluminous to felsic-peraluminous.

4.1.2. *Major-element contents*

As previously mentioned, the São Jorge and the Chapéu do Sol deposits are associated with both magmatic sequences, however, due to the lack of younger samples, our models for both deposits will concern only OMS. Harker diagrams for the OMS show that intermediate samples tend to scatter more strongly than the acid members and, for silica values over 65%, the trend is linear. Geochemical modelling shows that fractional crystallization accounts for the geochemical variability within OMS, which is characterized by three main petrologic trends. Within the higher silica side ($SiO_2 > 65$ wt%), one of trends accounts for part of the Patrocínio and Tocantinzinho samples. It starts from a granodioritic melt that fractionates plagioclase, pyroxene, biotite, magnetite and titanite, with a monzo-diorite cumulate (green array in Fig. 6). The other silica richer trend is characterized by a tonalitic initial composition and involves fractionation of albitic plagioclase, amphibole, biotite, magnetite and titanite (red array in Fig. 6), and is also compatible with a monzo-diorite cumulate. This trend encompasses most of the OMS, including the Tocantinzinho, Coringa, Chapéu do Sol, São Jorge (older) granite and part of the Patrocínio samples. The lower silica spectrum involves syenites and monzonites from the Patrocínio deposit and a few Tocantinzinho and Coringa samples that evolved through fractionation of K-feldspar, plagioclase, biotite, apatite, clinopyroxene and ilmenite (gray array in Fig. 6).

Samples from the YMS, particularly the intermediate rocks, scatter more strongly than the OMS on the Harker diagrams (Fig. 7). Three trends accounts for the petrologic evolution of the YMS. Intermediate V3 volcanics show an evolution coherent with a lati-andesite initial liquid that fractionates K-feldspar, amphibole, anorthitic-plagioclase and biotite (yellow array in Fig. 7), and generates a quartz-latite liquid and a diorite cumulate. The acid members of the V3 deposit define a trend compatible with a rhyolitic initial composition that differentiates to alkali-rhyolite through fractionation of albitic-plagioclase, K-feldspar, pyroxene and titanite, with a syenite cumulate (yellow array in Fig. 7). A relatively similar trend comprises the Batalha and Palito granitoids (black array in Fig. 7). This evolution starts from a granitic composition and is consistent with extraction of albitic-plagioclase (44%), K-feldspar (42%), pyroxene (7%), titanite (3%) and apatite (4%), generating an alkali-granitic liquid and a syenite cumulate.

4.1.3. *Trace-element contents*

REE spidergrams reveal similar patterns for OMS samples, characterized by a moderate level of HREE depletion (average $La/Yb_N \geq 12.1$, Fig. 8a–e). The steepest pattern was identified for the São Jorge deposit,

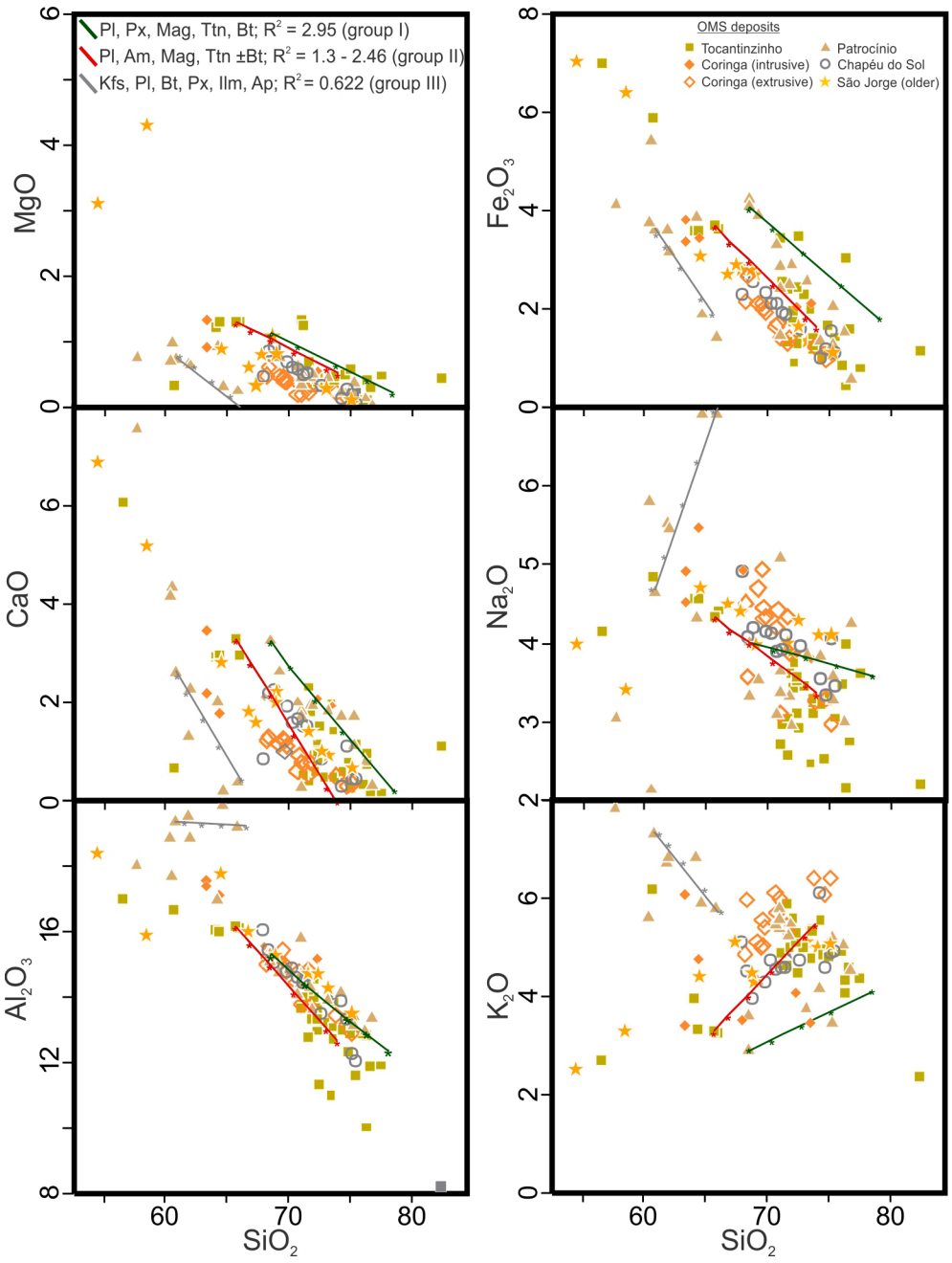

Fig. 6. Silica vs. major oxides diagrams for OMS rocks (symbols are the same as in the previous figures). Red, green and gray arrays mark the petrologic trends modeled with the respective minerals involved. The accuracy of the models is given by the R^2 parameter, which is defined by the sum of the differences between the theoretical and real differentiated melts for each element squared. Abbreviations: Am (amphibole), Pl (plagioclase), Bt (biotite), Px (pyroxene), Mag (magnetite), Ttn (titanite), Ap (apatite), Ilm (ilmenite).

in both older and younger granites (Fig. 8a) with averages La/Yb_N of 35.4 and 81.5 respectively, that are accompanied by positive to mildly negative Eu anomalies. The Patrocínio samples (Fig. 8b) also define a steep slope, yet more subtle than the older São Jorge granite, and are accompanied by null or moderately negative Eu anomalies. The Chapéu do Sol, Coringa and Tocantinzinho deposits (Fig. 8c–e) are characterized by less fractionated trends (average $(La/Yb)_N$ ratios of 19.5, 18.8 and 12.1 respectively) and slight to moderately negative Eu anomalies.

REE spidergrams for the YMS (Fig. 8f–h) show a much more subtle fractionation between light and HREE when compared with the older sequence (except for the younger São Jorge granite, Fig. 8a). The Eu anomalies are more restrict and vary from moderately negative to strongly positive. The V3 volcanic rocks show a moderate degree of fractionation (Fig. 8f, with average $(La/Yb)_N$ of 17.4) and moderately negative to negligible Eu anomalies. The Palito and Batalha deposit rocks behave similarly (Fig. 8g and h, average $(La/Yb)_N$ ratios of 10.9 and 8.1 respectively) and define smoother trends towards lower HREE contents, with moderate to strongly negative Eu anomalies. The trace-element spidergram (Fig. 8i) shows that YMS is slightly enriched in HFSE (Ti, Dy, Y, Zr, Sm) and show lower Sr contents.

Fig. 9 shows trace-element ratios plotted against maficity (Fe + Ti + Mg calculated for millications) or Eu anomaly calculated as Eu_N/Eu^* (Eu_N = concentration of Eu normalized by the chondrite after Boynton (1984); $Eu^* = \sqrt{Sm_N.Gd_N}$). On the Dy/Yb vs. maficity plot for the older sequence (Fig. 9a) it's clear that the older São Jorge granite is the unit with the largest range of Dy/Yb, and is followed by the Tocantinzinho and Chapéu do Sol samples that show a minor spread between $1 \leq Dy/Yb \leq 2$. The Patrocínio and Coringa samples don't vary significantly and show Dy/Yb ratio around 2. The younger sequence shows a similar trend and spread horizontally on the plot, with maficity values between 10 and 200 for a Dy/Yb ratio around 2. The younger São Jorge granite stands as an outlier and shows Dy/Yb ratio from 2 to 4.

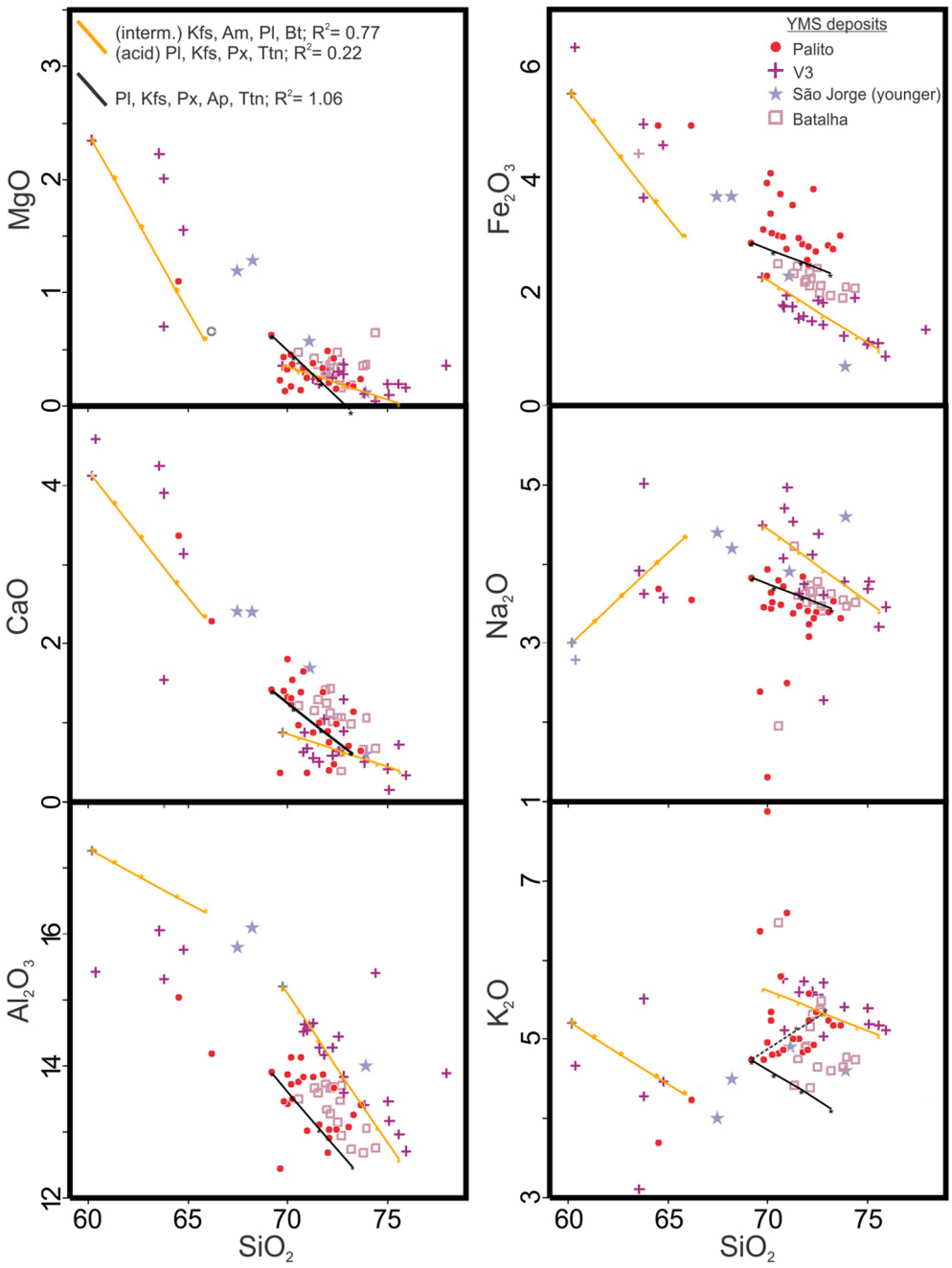

Fig. 7. Silica vs. major oxides for YMS rocks. Yellow and black arrays mark the petrologic trends modeled, with the minerals involved and the R^2 parameter indicated at the top. Symbols are the same as in the previous figures. Abbreviations: Kfs (K-feldspar), Am (amphibole), Pl (plagioclase), Bt (biotite), Px (pyroxene), Ttn (titanite), Ap (apatite).

The Sr/Y vs Eu_N/Eu^* diagram (Fig. 9b) shows a positive correlation between the two parameters. In general terms, the Patrocínio, Coringa, São Jorge and Chapéu do Sol show predominantly moderate Sr/Y values that fall between 5 and 50. The only sample cluster was identified for the Tocantinzinho deposit, that shows predominantly low ratio ($Sr/Y \leq 5$), with scarce exceptions. A similar behavior was identified for the younger Batalha and Palito granitoids, with Sr/Y ratio ≤ 5. On the other hand, V3 volcanics and the younger São Jorge granite samples show moderate to high ratios ($Sr/Y \geq 50$) followed by null or positive Eu anomalies.

Both older and younger igneous sequences can be separated into low, moderate and rarer high La/Yb rocks. On average, the La/Yb and Eu_N/Eu^* correlate positively. For the OMS, Fig. 9c shows that the São Jorge samples vary from moderate to high ratios ($30 \leq La/Yb \leq 100$). The Coringa, Patrocínio and Chapéu do Sol samples show predominantly moderate values ($20 \leq La/Yb \leq 50$), whereas the Tocantinzinho deposit shows mainly low La/Yb rocks (≤ 20). For the younger sequence, the São Jorge granite shows the highest La/Yb ratios (>100), which is accompanied by the highest Eu_N/Eu^*. Moderate values ($20 \leq La/Yb \leq 50$) were acquired for the V3 volcanic units, whereas the Batalha and Palito granitoids show the lowest ratios ($La/Yb \leq 20$).

In summary, OMS shows a wide compositional range and rocks vary from magnesian to slightly ferroan, alkali-calcic to calc-alkalic, metaluminous to moderately peraluminous and show steep REE patterns. Three trends accounts for the OMS evolution: a magnetite and pyroxene bearing one involving granodiorites and granites; an amphibole and magnetite one that comprises most OMS-hosted deposits; and a third one involving pyroxene and ilmenite fractionation on K-rich magmas. YMS

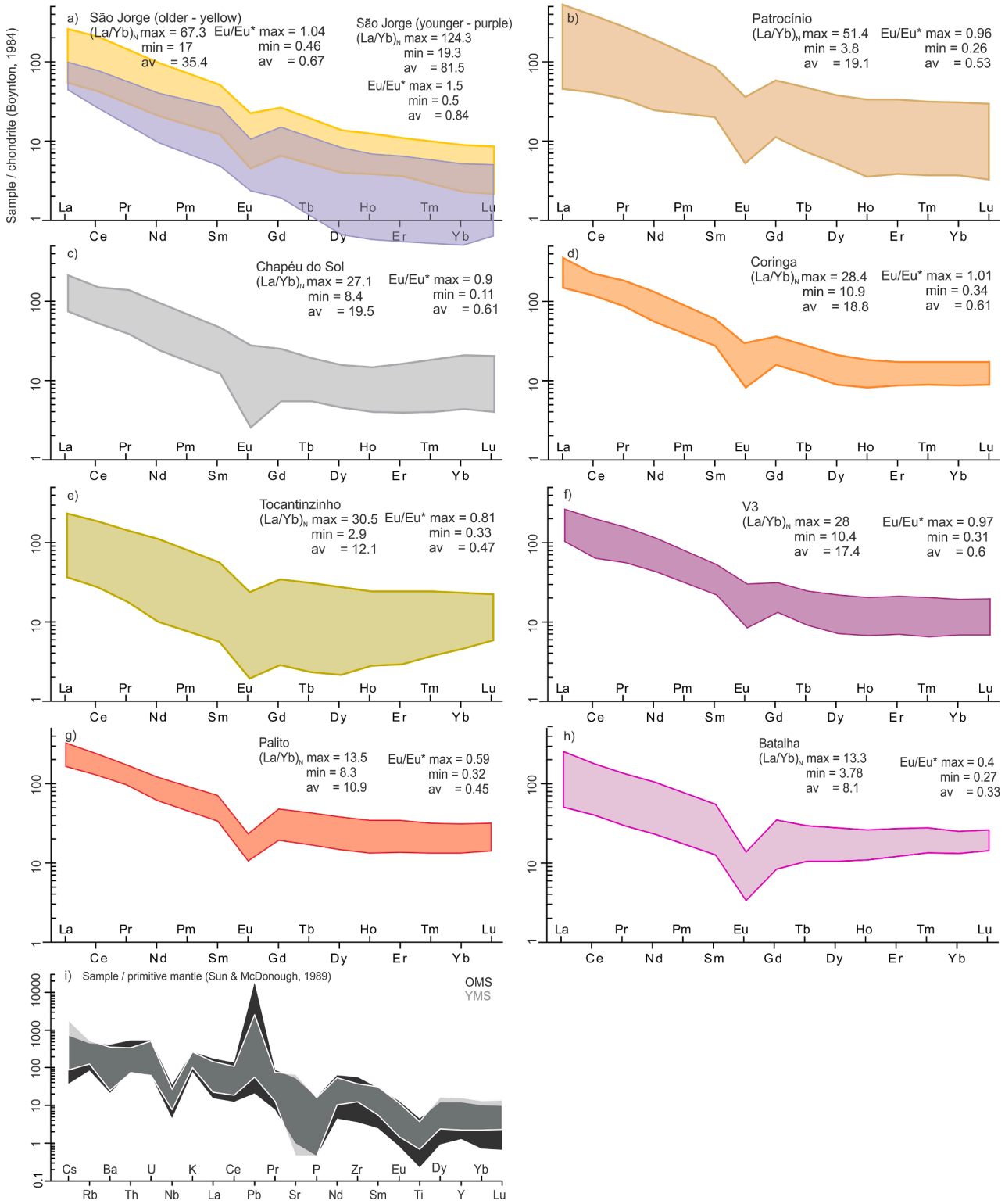

Fig. 8. Chondrite normalized (Boynton, 1984) REE spidergrams for the OMS (a – e), YMS (f – h) and trace-element spidergrams normalized by the primitive mantle (Sun and McDonough, 1989) for both sequences. The respective colored fields represent the entire range covered by each deposit/unit. Eu anomaly calculated as $Eu/Eu^* = Eu_N/\sqrt{(SmN.GdN)}$.

shows similar MALI and aluminosity, however with a more restrict compositional range and more subtle REE patterns on essentially ferroan samples (excepted for intermediate V3). Our models show that these rocks evolved on an reduced and predominantly anhydrous trend.

4.2. Zircon geochemistry

4.2.1. Morphology and textural description

At this study we present three new geochronology results and reexamine two samples (USP14-136 and USP14-160) presented by Cassini et al. (2020) for inheritance. Invariably, all zircon analyses refer to OMS

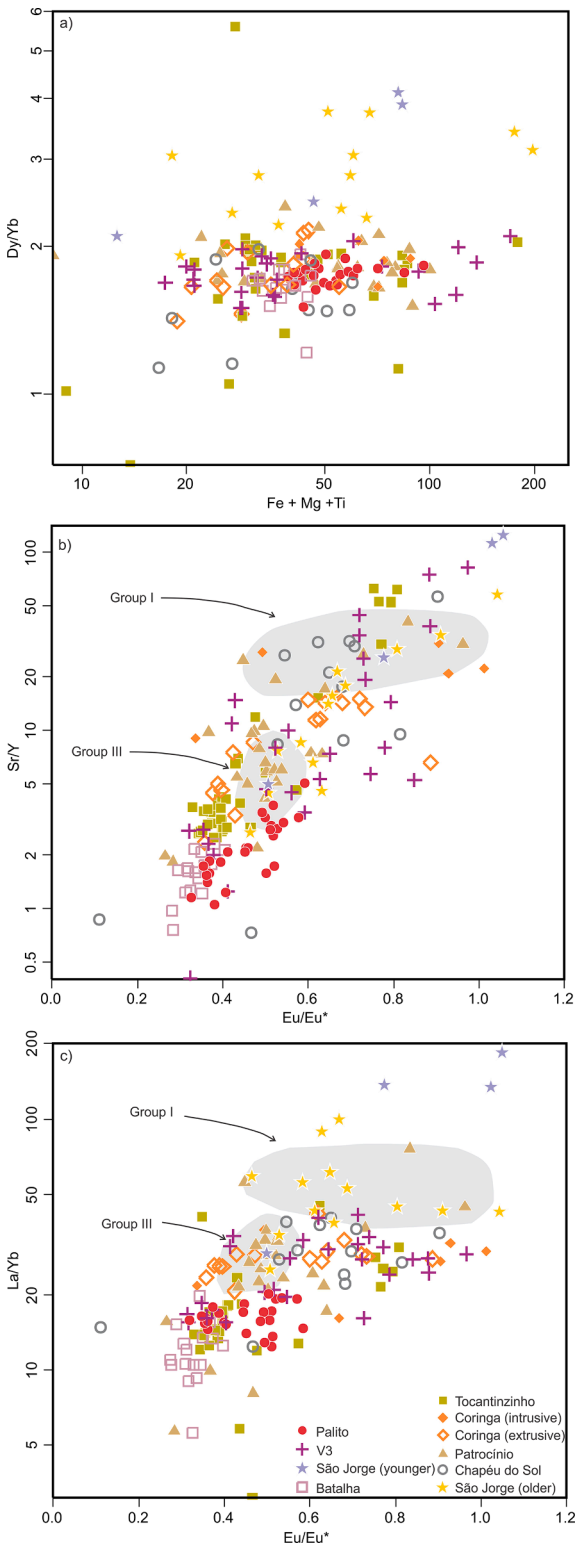

Fig. 9. Maficity vs. Dy/Yb (a), Eu/Eu* vs. Sr/Y (b) and Eu/Eu* vs. La/Yb (c) plots for OMS and YMS. Dy/Yb ratio is strongly influenced by amphibole as the mineral shows high Kd's for both elements. Sr/Y and La/Yb might also be influenced by amphibole, however, plagioclase and pyroxene on a lesser extent might also shift the ratios towards higher or lower values.

samples collected on the surroundings of the Patrocínio village, in central TMP. Sample USP14-160 (granodiorite) is characterized by subhedral grains, with rounded or partially corroded edges, 2:1 elongation ratio, with predominantly oscillatory but also broad and patchy zonings. Round shaped xenocrystic cores displaying both dissolution and resorption textures are also common (Fig. 10a). Sample USP14-144 (granodioritic porphyry) is dominated by euhedral to subhedral, elongated grains (between 2:1 and 3:1), with oscillatory and less frequent patchy and sector zonings. Two types of cores are observed on this sample: one comprises rounded, partially resorbed xenocrystic cores (Fig. 10b), commonly fractured and metamictic; and the other, comparatively more frequent, is characterized by oscillatory or homogenously zoned nuclei and lacks dissolution or resorption textures. Sample USP14-83, an aplite dyke of syenitic composition (R1-R2 classification), comprises euhedral and subhedral zircon grains, with 2:1 elongation and well preserved oscillatory zoning (Fig. 10c). Round-shaped, partially resorbed xenocrystic cores with homogeneous, patchy or sector zonings are also observed. Sample USP14-91 represent a coarser-grained syenite and is characterized by subhedral to anhedral grains, with elongation that varies between 1:1 and 2:1 (rarer 3:1 grains), predominance of oscillatory zoning with minor examples of sector and patchy zonings. Cores show predominantly oscillatory and, less frequently, homogenous zonings with rarer xenocrystic and metamictic domains (Fig. 10d). Sample USP14-136 (monzonite) is composed by euhedral to subhedral grains, with elongation between 2:1 and 3:1, with well preserved oscillatory and sector zonings. A detailed evaluation and description of the grains allowed the identification of two types of cores: rounded xenocrystic cores that commonly display dissolution textures and zoning patterns that truncates the rim (Fig. 10e); and comparatively homogenous rounded cores that show concordant zoning patterns.

4.2.2. U-Pb dating (LA-ICP-MS)

The granodiorite sample (USP14-160) presents a continuous distribution of $^{207}Pb/^{206}Pb$ ages between 2000 and 2100 Ma, as demonstrated by the frequency histograms from Fig. 10a, with a more pronounced peak at ca. 2020 Ma. Autocrystic cores were evaluated and yielded concordant ages of 2031.2 ± 2.0 Ma (n = 15), whereas 6 xenocrystic cores revealed ages higher than 2050 Ma. Rims analyses yielded 2011.7 ± 4.5 Ma (n = 13) understood as the sample's magmatic age.

The granodioritic porphyry (USP14-144) presents $^{207}Pb/^{206}Pb$ ages that spread from 1800 to 2040 Ma, with a more pronounced peak at ca. 1980 Ma (Fig. 10b). Five xenocrystic cores were analyzed and yielded concordant results that converge to 2010.9 ± 8.1 Ma. Autocrystic cores and rims point to similar ages, and 22 grains align on a discordia with upper intercept at 1986.9 ± 5.9 Ma, considered as the samples magmatic age.

For the aplitic syenite sample (USP14-83) $^{207}Pb/^{206}Pb$ age histograms (Fig. 10c) shows that results concentrate at ca. 1990 Ma, with minor older and younger examples. A total of 15 xenocrystic cores were evaluated and defined a discordia with upper intercept at 2012.7 ± 6.7 Ma. Core and rim analyses yielded discordant results and 16 grains align on a discordia with upper intercept at 1987.3 ± 7.1 Ma, interpreted as the magmatic age.

The syenite sample (USP14-91) also shows $^{207}Pb/^{206}Pb$ ages clustered at ca. 1990 Ma (Fig. 10d). Cores and rims analyses converge to a concordia age of 1993.7 ± 2.7 Ma (n = 11). Xenocrystic cores are rare in this sample and were not evaluated.

The monzonite sample (USP14-136) shows $^{207}Pb/^{206}Pb$ ages that spread between 1900 and 2060 Ma, with a clear cluster at ca. 1980 Ma (Fig. 10e). Twelve xenocrystic cores were analyzed and yielded discordant ages that roughly align on a discordia with upper intercept at 2055.5 ± 8.7 Ma. Cores and rims analyses revealed 18 grains that converge to a concordia age of 1974.6 ± 1.9 Ma, understood as its magmatic age.

4.2.3. Trace element contents

Zircon Eu anomalies are constrained on the diagram from Fig. 11a, where Eu/Eu* is plotted against Zr/Hf (as a proxy for differentiation). At a first glance, all samples show predominantly Eu/Eu* < 0.5, with a few

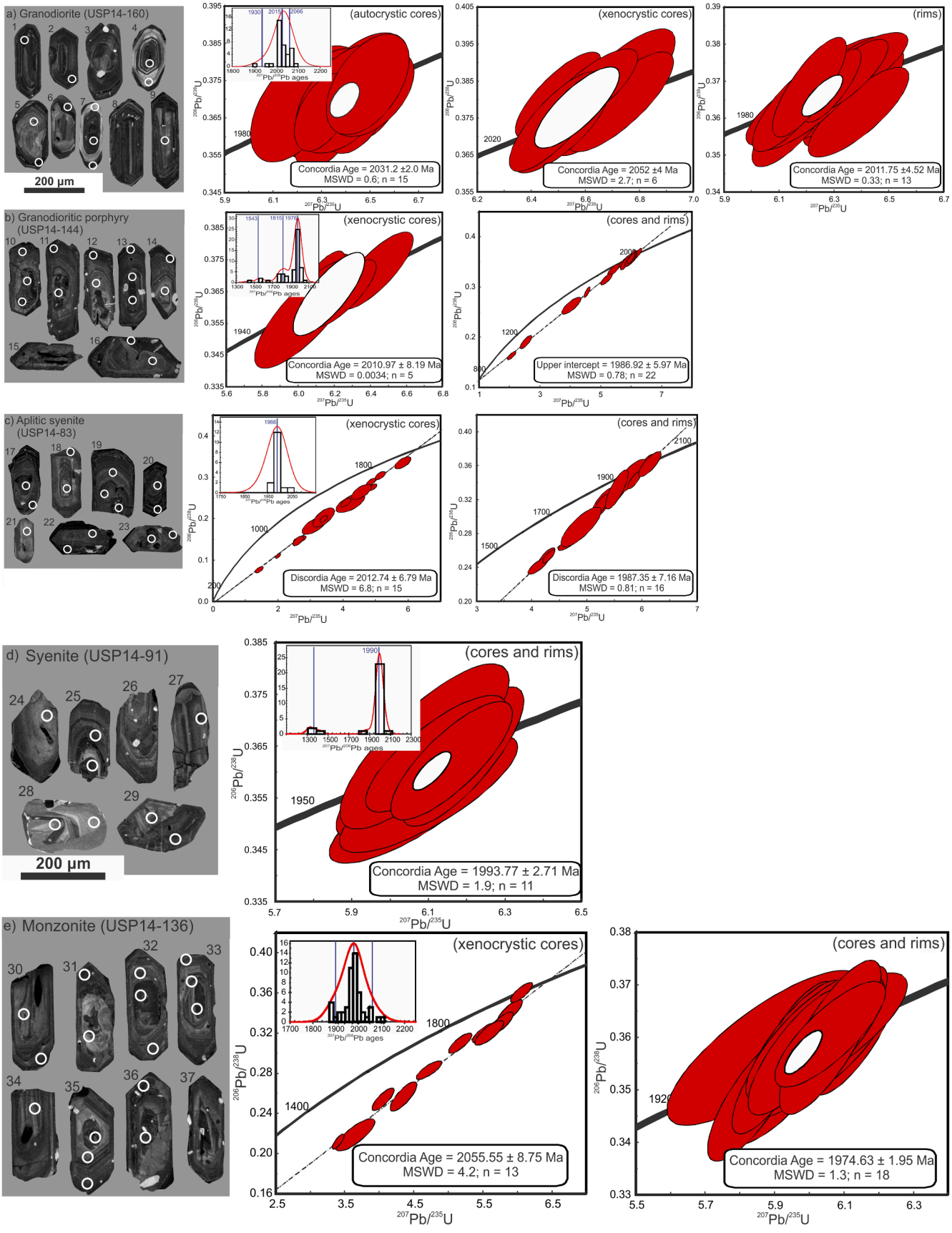

Fig. 10. Cathodoluminescence images from selected zircon grains and the respective concordia-discordia diagrams from the samples analyzed in this study. Spots are 20 µm wide. 1–3, 10, 11, 17–19 (partially dissolved) and 30–32 show inherited xenocrystic cores (grain 32 is partially resorbed); 4, 5, 14, 20, 25, 26 and 35 show oscillatory zoning; 6 and 7 are broad zoned grains; 8, 9, 15 and 27 show patchy zoned zircon grains; 12, 13, 33 and 34 show autocrystic cores; 16, 22, 23, 28, 29, 36 and 37 show sector zoning; 21 and 24 are homogeneous zoned.

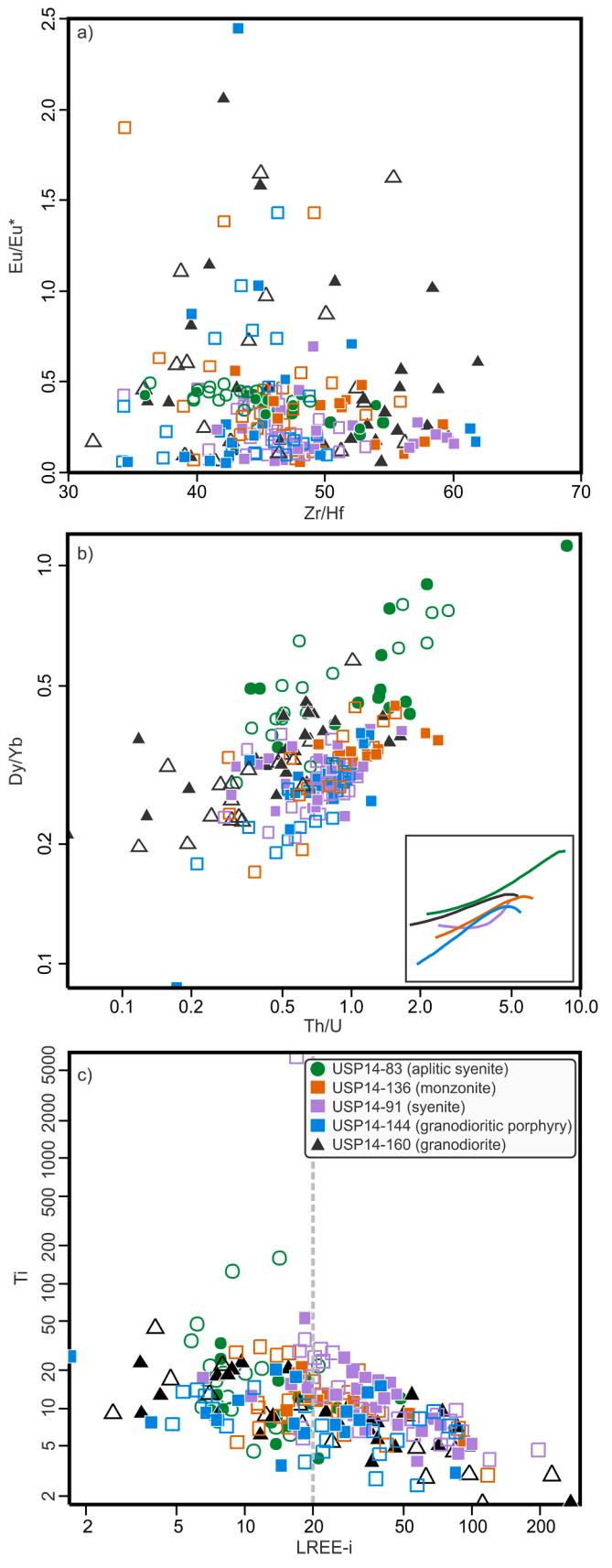

(caption on next column)

Fig. 11. Zircon geochemistry with Zr/Hf vs. Eu/Eu* (a) and Th/U vs. Dy/Yb plots (b), where both Zr/Hf and Th/U ratios were used as proxies for differentiation. Bottom right smaller graph in (b) shows the polynomial regressions with the general trend for each sample. (c) Light REE index (LREE-i) as proposed by Bell et al. (2016) vs. Ti plot. The index is calculated as LREE-i = (Dy/Nd + Dy/Sm), in order to constrain the proportion between middle and light-REE in zircon grains. Grains with low LREE-i show high LREE content, which might indicate hydrothermal alteration (or LREE rich inclusions such as apatite or monazite on the ablated spot).

exceptions for USP14-136, 144 and 160. Accordingly, samples USP14-91 and 144 cover a similar range and Eu/Eu* varies from 0.1 to 0.5, with a few values closer to unity or higher. Sample USP14-136 defines a gentle negative trend on the diagram, with core Eu/Eu* between 0.1 and 0.5, and 0.25 to 0.7 for the rims, with minor values>1. USP14-83 also defines a subtle negative trend, with Eu/Eu* varying from 0.25 on the cores to 0.5 on the rims as Zr/Hf decreases. Grains from sample USP14-160 scatter on the plot and Eu/Eu* ratio varies from 0.1 to 2.0, without any noticeable trend. The most prominent feature regards the higher Zr/Hf ratio acquired for zircon cores.

The Th/U vs. Dy/Yb plot marks how the zircon grains from all samples evolved regarding middle- and HREE fractionation and, accordingly, all samples define a positive trend (Fig. 11b) and zircon cores show higher Dy/Yb and Th/U than the rims. Sample USP14-83, despite having the most scattered pattern, shows the highest values for both ratios and grains plot on the upper right part of the graph (Dy/Yb varies from 0.4 to 1.0 and Th/U from 0.5 to 10). Samples USP14- 91 and 144 distribute similarly and Dy/Yb varies from 0.4 on the cores to 0.2 on the rims as Th/U falls from 1.2 to 0.4 (steeper pattern for USP14-144). Samples USP14-136 and 160 define sub parallel trends, the later characterized by lower Th/U ratios as Dy/Yb decreases from 0.4 on the cores to 0.2 on the rims.

The plot from Fig. 11c shows the LREE-index (LREE-I = Dy/Nd + Dy/Sm), as proposed by Bell et al. (2016), plotted against Ti. The parameters correlate negatively and, for LREE-I values>20, the trend shows a clearer linearity. Roughly all grains from sample USP14-83, and significant proportion of samples USP14-160, 144 and 136 plots on the scattered part of the graph (LREE-I < 20). Zircon grains from sample USP14-91, on the other hand, behave more linearly and plot predominantly on the right side of the graph (LREE-I > 20).

4.2.3.1. Ti-in-zircon thermometry. The Ti-in-zircon (TZirc.Ti) thermometer after Ferry and Watson (2007) was applied to constrain magmatic temperatures and the results are summarized on Table 3 (values below 620 °C and above 970 °C were discarded and not considered on our database). The plot from Fig. 12a shows how TZirc.Ti and zircon saturation temperature (TZirc.Sat) (Watson and Harrison, 1983) relate for each sample/grain analyzed and, accordingly, results distribute in three fields: i) upper part of the plot where TZirc.Ti > TZirc.Sat + 100, hence zircon-undersaturated field; ii) shaded area between 1:1 and 1:100 ; and iii) bottom part of the plot with TZirc.Ti < TZirc.Sat, zircon-oversaturated field. Whereas autocrystic zircons will plot on the bottom and eventually on field ii, inherited grains (ante- and xenocrysts) spread through all fields.

Samples USP14-144 and 160 show the lowest magmatic temperatures (medians of 768 °C and 782 °C respectively) with a broader distribution for the later, and are characterized by intermediate TZirc.Sat (794 °C and 798 °C respectively). Zircon grains distribute between fields ii and iii, with greater concentrations for the TZirc.Ti < TZirc.Sat field. Samples USP14-91, 136 and 83 show progressively higher magmatic temperatures, and median TZirc.Ti are respectively 786 °C, 811 °C and 818 °C. The first two show grains that equally distributed between fields ii and iii, with intermediate and high TZirc.Sat (793 °C and 819 °C respectively). Sample USP14-83 differs from the others and its zircon grains distribute essentially on fields i and ii, and are accompanied by the lowest TZirc.Sat (754 °C).

Table 3
Summary of zircon saturation temperature (T.Zirc.Sat), Ti-in-zircon thermometer (T.Zirc.Ti) and magmatic fO_2 values acquired for OMS.

Samples	T.Zirc.Sat (1) (°C)	T.Zirc.Ti (2) (°C)					log fO_2 (3)				
		Min	Q1	Q2	Q3	Max	Min	Q1	Q2	Q3	Max
USP14-160	798	674	717	734	783	818	−20.9	−18.1	−17.1	−15.6	−14.4
USP14-144	794	715	749	760	767	796	−16.2	−15.9	−15.1	−13.9	−12.2
USP14-83	754	705	762	794	813	864	−13.4	−12.0	−10.8	−9.5	−5.1
USP14-91	793	700	732	767	775	787	−17.3	−16.3	−15.2	−14.7	−14.0
USP14-136	819	725	763	787	807	820	−16.9	−15.6	−15.1	−14.3	−13.5

(1) Watson and Harrison (1983); (2) Ferry and Watson (2007), absolute error of ± 30 °C; (3) Smythe and Brenan (2016), propagated uncertainty of ± 1.2 log units.

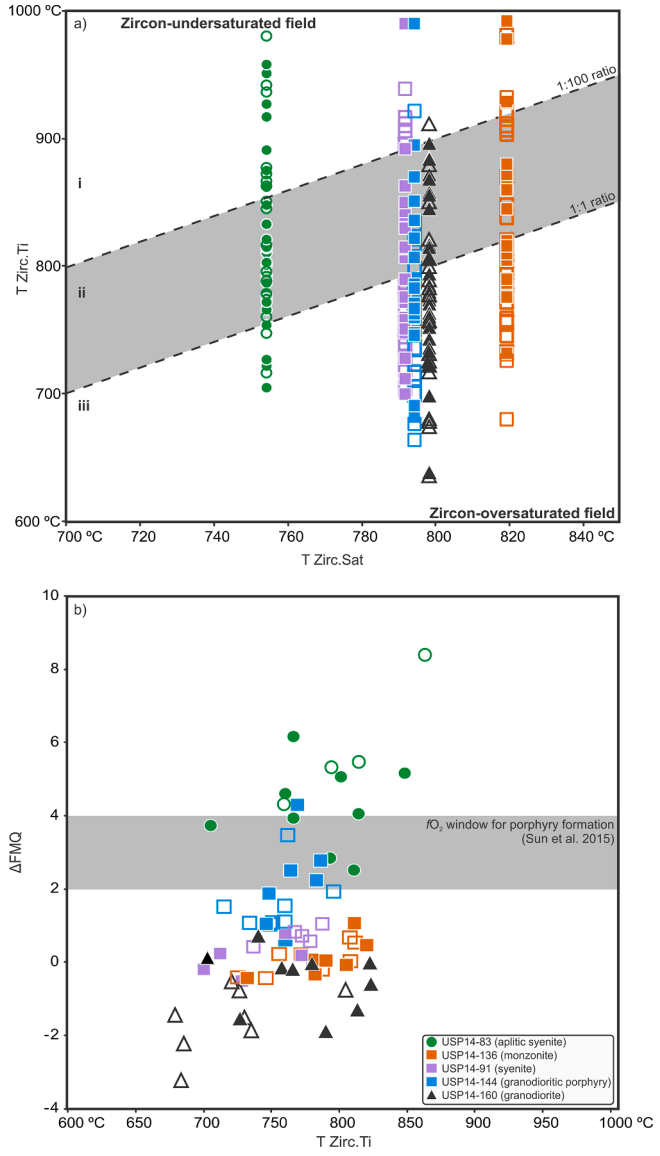

Fig. 12. Zircon saturation temperature (Watson and Harrison 1983) vs. Ti-in-zircon temperature (Ferry and Watson 2007) plot. The plot separates fields where zircon saturation is not achieved by the hosting magmas (top of the diagram) and, conversely, fields where zircon might be extracted from the magmas (center and bottom parts). Inherited grains might plot in all fields, whereas autocrystic grains will plot on the center and bottom parts. (b) Magmatic fO_2 treated as log units above or below the fayalite-magnetite-quartz oxygen buffer plotted against magmatic temperature (T Zirc.Ti).

4.2.3.2. Magmatic fO_2 estimates. In order to make the data easier to read and comparable with other paper's datasets, we treat magmatic fO_2 in log units above or below the fayalite-magnetite-quartz (FMQ) oxygen buffer (results are summarized on Table 3). The graph from Fig. 12b shows magmatic temperature (TZirc.Ti) plotted against ΔFMQ (xenocrysts, high La and low LREE-i zircon grains were ruled out). Sample USP14-83 shows the highest fO_2 values and zircon grains plot on the top part of the graph (values higher than ΔFMQ + 4). However, these results should be treated cautiously, as the sample shows predominantly low LREE-i zircon grains. The granodioritic porphyry (sample USP14-144) shows the second highest fO_2 values, with ΔFMQ from 0 to + 4. Samples USP14-91 and 136 cover a similar and narrower fO_2 range, with ΔFMQ between −1 and +1. Sample USP14-160 is characterized by the widest fO_2 range and samples tend to scatter more strongly (ΔFMQ varies from – 4 to 0) with a cluster between −2 and 0.

5. Discussion

5.1. A petrogenesis perspective: Generating the older and younger magmatic sequences

In the Tapajós Mineral Province, a clear feature of the OMS (igneous suites of 2.00–1.95 Ga) is its wider compositional range when compared with the YMS (igneous suites of 1.90–1.86 Ga, Fig. 4a and b). Yet, an interesting and relevant common ground for both magmatic sequences is the presence of metaluminous samples with higher maficity values (with exception of the Batalha granitoids as shown in Fig. 5c). The balance between Al and Na, Ca and K is particularly important in granitic rocks geochemistry as it efficiently constrains their petrogenesis (Clemens et al., 2011; Clemens and Stevens, 2012; Frost et al., 2001; Frost and Frost, 2013, 2011; Moyen et al., 2017; Villaseca et al., 1998) and, as such, it indicates metaluminous mafic sources for both OMS and YMS. Differences between the magmatic sequences are better evidenced on the Fe-index and MALI vs. silica diagrams (Fig. 5a and b) and major-oxides plots (Figs. 6 and 7), which suggests contrasting melting conditions and magmatic evolution, in spite of similar sources.

OMS rocks might be divided into three categories. Group I granitoids correlates with the Cuiú-Cuiú Complex, are found on the Patrocínio and Tocantinzinho deposits (southern and central TMP respectively), show slightly higher silica contents, are peraluminous, magnesian to ferroan, calc-alkalic to calcic and comprises granites and granodiorites compatible with mafic and oxidizing sources, with moderate to strong continental crust contribution. The group comprises the oldest granodiorite (sample USP14-160) dated in this contribution at 2011 Ma, characterized by a magnetite bearing and amphibole-free evolution (green array in Fig. 6) generating the horizontal distribution of samples on the Dy/Yb plot the moderate to low Sr/Y and La/Yb ratios (Fig. 9). These rocks represent the first batches of magmatism upon the onset of subduction on the TMP at ca. 2.0 Ga, that according to Cassini et al. (2020) is characterized by a strong crustal component due to incorporation of trench derived sediments and/or subcrustal-erosion of the subducted plate ($\varepsilon Nd_{(T)}$ of −8.36 acquired by the authors).

Group II granitites (s.l.) predominates at the TMP as a whole and correlates with the Creporizão Intrusive Suite. It comprises samples from the Tocantinzinho, São Jorge (older granite) and Chapéu do Sol gold deposits (northern and central TMP), with a few examples from the Patrocínio deposit (sample USP14-144 dated at 1986 Ma). The rocks are

metaluminous to mildly peraluminous, magnesian to slightly ferroan, calc-alkalic to alkali-calcic and suggest mafic to intermediate, oxidizing sources typical of subduction-related, I-type granites. Geochemical modelling demonstrates fractional crystallization as the main differentiation mechanism and a hydrous and oxidized trend consistent with plagioclase, amphibole, biotite, magnetite and titanite (red array in Fig. 6). Middle-REE depletion (clearer for the Tocantinzinho samples, Fig. 8) and the distribution on the Dy/Yb, Sr/Y and La/Yb plots (Fig. 9) confirms the role of amphibole. Samples from the Coringa deposit (southern TMP) plot on the magnesian-ferroan transition and are predominantly alkalic, compatible with highly differentiated I-type granites (Frost et al., 2001; Frost and Frost, 2011). In addition, these samples cover the higher silica spectrum of group ii's trend (red array in Fig. 6), suggesting a similar petrologic evolution. Considering the more discrete variation on the Dy/Yb, Sr/Y and La/Yb ratios, amphibole most likely played a lesser role on the evolution of the Coringa rocks. As a whole, group ii rocks might be might be understood as differentiated, I-type granites that represent the evolution of the arc-magmatism.

Group III comprises lower silica, K-rich ($K_2O > 5$ wt%), metaluminous to peraluminous, ferroan and alkalic syenites and monzonites with ages between 1974 and 1993 Ma. Major- and trace element patterns show that group III derives from anhydrous, metasomatized, mafic and reducing parental magmas with restrict crustal contribution ($\varepsilon Nd_{(T)}$ from −1.64 to + 1.69 acquired by Cassini et al., 2020). The authors also demonstrated how these rocks evolved on an anhydrous and reduced petrologic trend (pyroxene and ilmenite bearing) as a consequence of corner flow induced, decompression mantle melting. Early extraction of plagioclase is symptomatic of anhydrous melts and explains the Eu anomalies (negative), Sr and Ba depletions, and low Sr/Y and La/Yb ratios. This group of rocks, that accounts for about 15% of our database and encompasses Patrocínio, Tocantinzinho, Coringa and São Jorge samples, is not constrained on the S-I-M-A classification (Chappell and White, 2001) and it is often treated as K-rich calc-alkaline granitoids (Bonin, 2004, 1990; Bonin et al., 2020) or as Fe-K granitoids (Laurent et al., 2014) that are typical of post-orogenic or collisional tectonic settings (Bonin, 2004; Frost et al., 2001; Liégeois et al., 1998). Despite their abundance in Proterozoic terrains throughout the world (Bogaerts et al., 2006; Ferré et al., 1998; Ferreira et al., 1998; Kouankap Nono et al., 2010; Laurent et al., 2014; Vander Auwera et al., 2011), the precise petrogenetic mechanism behind high-K, metaluminous and ferroan granitoids is still debatable.

Within the YMS, V3 volcanics (Iriri Group) vary from metaluminous to peraluminous, alkalic to calc-alkalic and are magnesian on the lower silica side and ferroan on the more acid members, geochemical attributes that suggest oxidizing to reducing mafic parental magmas with contribution of preexisting crust. Geochemical modelling indicates that intermediate V3 (and the few younger São Jorge granite samples) evolved through K-feldspar, amphibole, anorthite-rich plagioclase and biotite extraction (yellow array in Fig. 7), yielding higher Dy/Yb, Sr/Y and La/Yb ratios (Fig. 9). More prominent differences between the older and younger sequences are evidenced by the acid V3 volcanics and by the Palito and Batalha granitoids (that correlate with the Parauari Intrusive Suite). The rocks show similar aluminosity with the OMS but are alkali-calcic, essentially ferroan, show a much narrower compositional range and evolved on a pyroxene and magnetite-free trend (black array in Fig. 7), characterized by lower Sr/Y, La/Yb and Eu/Eu* ratios. These geochemical attributes mark a transition from hydrous and oxidizing to anhydrous and reducing mafic sources.

As a whole, OMS and YMS show subtle geochemical differences and contrasting petrologic trends and these differences lend support to a changing tectonic framework on the TMP at ca. 1.88 Ga, from a magmatic-arc context to a post-orogenic or collisional setting (Juliani et al., 2005; Lamarão et al., 2005, 2002; Santos et al., 2004, Santos et al., 2001; Santos et al., 2000). The suppression of subduction and the absence (or low activity) of slab-derived fluids positions SCLM as the main magmatic source and explains the higher HFSE content of YMS.

5.2. Insights from zircon geochemistry: Examples from the Patrocínio gold mineralization

Whole-rock geochemistry shows that the OMS might be grouped into three categories: group i involves higher-silica granites and granodiorites that evolved on a dryer trend through fractionation of pyroxene, magnetite and titanite; group II involves granites (s.l.) and are compatible with extraction of amphibole, magnetite and titanite; and group III accounts for the low-silica, high-K syenites and monzonites that evolved on a pyroxene- and ilmenite-bearing trend. Zircon textural description and geochemical analyses for groups I, II and III reveal a protracted petrologic history of approximately 40 Ma.

Sample USP14-160 (granodiorite) belongs to group I, shows the oldest age among the rocks dated in this study (2011 Ma), autocrystic cores of 2031 Ma and xenocrystic cores of 2052 Ma, both characterized by higher Zr/Hf and Th/U than the rims (Figs. 10a, 11a and b). The abundance of inherited cores combined with the whole-rock $\varepsilon Nd_{(T)} = -8.36$ (Cassini et al., 2020) and the high TZirc.Sat (798 °C) supports the contribution of preexisting crust for the formation of group i magmas. A few grains stand as exceptions and show Hf-enriched cores, reflecting episodic injections of new magma batches as zircon crystallize. Partially corroded and rounded edges and the low whole-rock Zr content of this sample (179.6 ppm) suggest early zircon extraction. According to our models, this sample belongs to a magmatic series that evolved through profound extraction of plagioclase (~71% of the cumulate composition), and a strong negative Eu anomaly would be ubiquitous on the evolving melt. Loader et al. (2017) demonstrated how titanite fractionation might potentially drive the melt towards positive (or only subtly negative) Eu anomalies, as the mineral incorporates preferentially the other trivalent REE ($Kd^{REE3+}_{titanite} > 100$, Bachmann et al., 2005). Hence, the chemical effects of plagioclase extraction in group i granites is apparently counterbalanced by synchronous extraction of titanite (and less importantly pyroxene), which assigns the evolving magma and subsequently crystallizing zircon grains (or rims) their Eu/Eu* ≥ 0.5 and lower Dy/Yb ratios (Fig. 11a and b). Additionally, the preferential incorporation of Th by titanite explains the evolution towards lower Th/U (Harrison et al., 2007; Lee et al., 2021). Despite the compatibility with magnetite, the plot from Fig. 12b shows fO_2 values close to or a few log units below the FMQ buffer, just enough to stabilize the mineral.

The granodioritic porphyry (sample USP14-144) belongs to group II granitoids and is characterized by magnetite, titanite and amphibole fractionation, a magmatic age of 1986 Ma and rounded, partially corroded inherited xenocrystic cores dated at 2010 Ma (Fig. 10b), compatible with group I ages. Zircon morphology (3:1 elongation) and the synchronicity of core and rims suggest a rapid crystallization history for this sample, which is compatible with the shallower crustal level expected for a porphyry intrusion. Profound extraction of plagioclase (~73% of the cumulate) explains the evolution towards lower Eu/Eu* as Zr/Hf decreases and, the few samples with higher Eu/Eu* likely reflects competing titanite extraction. However, differently than sample's USP14-160 case, titanite is approximately 4 times rarer within group II's petrologic trend, fact that diminishes significantly its geochemical effects on the evolving melt. Combined fractionation of titanite and amphibole modeled for group II yields the steepest array on the Th/U vs Dy/Yb plot and the lowest magmatic temperature (768 °C) acquired in this study. In addition, the oxidizing condition of this sample is sustained by geochemical modelling and by fO_2 values between ΔFMQ + 0 and ΔFMQ + 4.

Samples USP14-83, 136 and 91 (syenites and monzonites) belong to the high-K series (group III) that is characterized by a dry, reduced and protracted magmatic history. USP14-91 marks the onset of the high-K magmatism at ca. 1993 Ma (Fig. 10c). This sample presents low silica contents (~60 wt%) and zircon stabilization is likely due to the high whole-rock Zr (357.7 ppm) (Fig. 12a indicates the predominance of autocrystic grains). Sample USP14-136 shares similar characteristics,

yet, much younger magmatic age (1974 Ma, Fig. 10d), representing a late stage pulse of the high-K magmatism. Inherited zircon grains dated at 2055 Ma reflects a longer period of residence on deeper hot zones by these primary magmas (Annen et al., 2006), adequately explaining the positive to slightly negative $\varepsilon Nd_{(T)}$ acquired for group III rocks (Cassini et al., 2020). Sample USP14-83 intrudes as synmagmatic aplitic dykes and represents the evolution of the high-K magmatism. Its low whole-rock Zr content (127.4 ppm) suggests that the magma underwent previous zircon extraction and, consequently, the 1987 Ma age (Fig. 10e) should be understood as inherited (Fig. 12a indicates the predominance of antecrystic zircon grains). This idea is supported by the incompatibility between our geochemical modelling results (that indicates a reduced petrologic trend) and the extreme high fO_2 values acquired for group III (Fig. 12b). The LREE index vs. Ti plot (Fig. 11c) indicates that USP14-83 and 136 in a lesser extent, are anomalously LREE enriched, reflecting either hydrothermal alteration or mineral inclusions on the ablated spot (Bell et al., 2019, 2016), which might compromise the reliability of the results. As a consequence, zircon trace-element contents for these rocks should be looked at cautiously. The Eu/Eu* values predominantly below 0.5 denies fractionation of titanite and the smoother drop on the Dy/Yb ratio as Th/U decreases negates amphibole extraction, supporting the dry, ilmenite- and pyroxene-bearing evolution modeled for group III. Its reducing affinity, as pinpointed by geochemical modeling, contrasts with fO_2 estimates of ΔFMQ + 0 to + 2, which evidences the interaction of group III and the synchronous group II magmas. Additionally, the higher magmatic temperatures acquired for group III syenites and monzonites (786°–811 °C) reinforce the dry characteristic of the high-K magmatism.

5.3. Fertile or not-fertile: The million dollar question

On a tectonic perspective, typical Cu – Au porphyry deposits form preferentially (but not only) in destructive plate margins where they genetically relate with hydrous (up to 6 wt% H_2O), oxidized (ΔFMQ + 0 to + 2), intermediate to acid, shallow, arc-related intrusions that upon decompression exsolves fluids and volatile phases responsible for mobilizing siderophile and chalcophile elements under chlorine- or sulfate-bearing complexes and, ultimately, for their precipitation as ore metals (Richards, 2015a, 2011a; Sillitoe, 2010; Sobolev and Chaussidon, 1996; Sun et al., 2015). Interestingly, not all arc rocks are adequate for the formation of porphyry deposits and, in this regard, hypotheses involving the depth of intrusion, size of the pluton, redox state and water, sulfur and metallic contents of the magmas have been raised as potential players that might influence whether or not a given magmatic system is fertile (a good summary might be found in Zhang and Audétat, 2017). Sulfur speciation, as a consequence of magmatic fO_2, stands as one of the most critical variable that dictates the characteristics of the porphyry mineralization (Sun et al., 2015). According to Richards (2015a), mantle melting in subduction zones under $fO_2 \geq$ ΔFMQ + 1 destabilizes residual sulfides and transfer their metallic content into the evolving melt. The optimal oxidation state, around ΔFMQ + 0 to + 2, may only be achieved through several million years of steady subduction. In essence, timing and tectonic context are crucial points to fully assess the metallogenetic potential of the igneous suites in the TMP.

The different igneous suites that encompass the OMS are interpreted as subduction related (e.g. Cassini et al., 2020; Juliani et al., 2002; Lamarão et al., 2005; Lamarão et al., 2002), and group i granitoids of ca. 2011 Ma represent the first batches of the arc-magmatism. These rocks are characterized by fO_2 values close to or below ΔFMQ, which are lower than the typical range for arc rocks (ΔFMQ + 0 to + 2). By combining its redox state with the pyroxene-bearing petrologic evolution, group i granites and granodiorites represent an unfertile stage of the arc-magmatism for the formation of typical Cu – Au magmatic-hydrothermal mineral deposits. In fact, group i rocks show negligible hydrothermal alteration (minor and localized K-metasomatism) and lack any trace of mineralization (Cassini, 2016).

Group II granitoids, identified in the Tocantinzinho, Chapéu do Sol, Coringa, São Jorge and Patrocínio deposits, show higher fO_2 (ΔFMQ + 0 to + 4) and a petrologic trend compatible with amphibole fractionation, characteristics that indicate the evolution of the arc-magmatism towards more hydrous, oxidized and metallogenetic fertile conditions. The granodioritic porphyry (USP14-144) dated at 1986 Ma is also accompanied by younger granitoids, evidencing a protracted magmatic history behind group II rocks (i.e. 1958 Ma for amphibole-bearing monzogranite from the Patrocínio deposit by Cassini (2016); 1979 Ma for the Tocantinzinho deposit syenogranites by Borgo et al. (2017); 1975 Ma for the Coringa deposit rhyolites by Tokashiki (2015)), a typical feature of porphyry forming plutons (Chelle-Michou et al., 2017; Large et al., 2018; Pirajno, 2009; Richards, 2015a). Group II-hosted mineralizations are defined by disseminated gold bearing sulfides or by pyrite-quartz ± gold ± chalcopyrite veins and veinlets most often found in the sericitic and, less frequently, in the potassic and propylitic alteration zones. Early and late stage hydrothermal alterations (sodic and argilic respectively), when present, are barren.

The high-K magmatism of group III covers an age interval of approximately 20 Ma (1993–1974 Ma) and represents decompression melting of metasomatized mantle. Group III rocks are rarer in the TMP, yet, syenites and monzonites have been reported in the Patrocínio, Tocantinzinho, Coringa and São Jorge gold deposits. Our fO_2 estimates between ΔFMQ − 1 to + 1, combined with the pyroxene-bearing petrologic trend, assigns this group a low favorability for the formation of Cu – Au magmatic-hydrothermal systems. Interestingly, group III rocks often show sericitic, potassic and carbonate hydrothermal alteration with disseminated, gold bearing, pyrite and pyrrhotite, features that we interpret as diagnostic of an interaction between the reduced, anhydrous and unfertile high-K magmas with the synchronous, hydrous, oxidized and metallogenetic fertile group II melts.

There is a lack of data when it comes to mineralization age in the TMP and, in spite of the theoretical fertility of group II granites (and group III on a minor extent), Ar-Ar dating of alunite crystals points to mineralization age of 1.86 – 1.84 Ga, which is compatible with the YMS (ages from the V3 and Batalha deposits by Echeverri Misas (2015) and Juliani et al. (2005)). Whereas OMS represents the magmatic-arc sequence with oxidized and hydrous melts, YMS is compatible with the evolution of the system towards late-orogenic and collisional tectonic settings, a consequence of the progressive flattening of the subducting-slab, resulting in progressively anhydrous and reduced magmas (Fernandes et al., 2011; Fernandes and Juliani, 2019). During active subduction, the continuous sulfur influx through the mantle enables a high fS_2, which stabilizes gold- and copper-rich residual sulfides. When subduction stalls, subsequent mantle melting (likely involving metasomatized SCLM), triggered due to astenospheric upwelling or orogenically thickened crust, will efficiently destabilize the previously formed sulfides and mobilize their metallic content into the generating melt (Richards, 2015a, 2011a). Hence the association of gold-rich porphyry deposits with late-orogenic or collisional magmatism such as the YMS (Chen et al., 2015; Hou et al., 2013; Richards, 2015b). The Batalha and Palito deposit (and possibly the younger São Jorge granite) are hosted by the Parauari Intrusive Suite that coupled with the volcanics of the V3 deposit (Iriri Group) represent the first batches of the YMS (ca. 1.89 Ga). The first two deposits show the greatest concentration of disseminated gold and gold bearing sulfide veinlets in the sericitic alteration zone and, secondarily, on the propylitic and argilic zones. The associated granitoids show features (metaluminous to mildly peraluminous, high-K to shoshonitic, more evolved Nd isotopes than OMS and > 2.0 Ga inherited zircon grains) that suggest a mutual role of metasomatized mafic and crustal sources (Cassini et al., 2020; Echeverri Misas, 2015; Santos et al., 2004). The V3 deposit is hosted by rhyolites compatible with a stronger crustal contribution in primary SCLM magmas (ferroan, peraluminous, alkali-calcic to calc-alkalic). Mineralization is found in hydrothermal breccias in a shallower stratigraphic level of the system, and consists on alunite- and gold bearing sulfide

veinlets distributed on the advanced argilic alteration, with lower sulfide concentrations on the potassic, propylitic and sericitic alterations.

In summary, despite their predominantly anhydrous characteristic, the first pulses of YMS are intimately related with gold-rich (gold-only?) magmatic-hydrothermal mineral deposits as a result of remobilization of SCLM and/or lower crust residual sulfides. Hence, the Parauari Intrusive Suite and the initial pulses of the Iriri volcanism may be considered as potentially fertile for the generation of gold-rich magmatic-hydrothermal mineral systems.

5.3.1. What the Sr/Y ratio tell us?

Over the past decade much attention has been driven to the relation between high Sr/Y rocks and porphyry Cu – Au deposits (i.e. most calc-alkaline, arc- and porphyry related magmas found in Andean-type subduction zones show high Sr/Y ratio), even though the origin of such relation remains in dispute. Some authors (e.g. Mungall, 2002; Sun et al., 2015) defend that high Sr/Y arc-rocks are genetically related with slab-melting and should be understood as high-silica adakites (Moyen 2009). However, thermal modelling of subduction zones (e.g. Bouilhol et al., 2015) reveals that slab melting is rare and unlikely to be a major contributor for arc-magmatism, neither is garnet an abundant restitic phase upon mantle melting. An alternative explanation suggests that the adakitic signature of arc-magmas relates with the magmatic evolution itself and relies primarily on the timing of amphibole and plagioclase fractionation (Chiaradia et al., 2012; Loucks, 2014; Richards, 2011b). High Sr/Y rocks experienced early amphibole extraction and is typical of magmas with $\geq$ 4 wt% H_2O that evolved at mid-crustal depths. On the other hand, if plagioclase precedes amphibole extraction, the case for less hydrous and shallower developed magmas, the system will be Sr depleted and the result will be low Sr/Y magmas.

More recently, special attention has been driven to alkaline, high-K to shoshonitic, low Sr/Y magmas, intruded in late- to post-subduction environments, the geologic scenario that frames TMP's context. World-known deposits such as Cadia Au – Cu porphyry (eastern Australia), the Bingham Canyon Cu – Mo – Au porphyry (eastern USA) and the Ok-Tedi Au – Cu porphyry (Papua New Guinea) are found in such geologic and tectonic contexts (Cloos et al., 2005; Cooke et al., 2014; Grondahl and Zajacz, 2017; Holliday et al., 2002; Richards, 2009). Chiaradia (2012) explains the Sr/Y ratio of a given magma with basis on the depth of evolution. Accordingly, intermediate composition magmas evolving at depths>0.2 GPa will stabilize amphibole prior to plagioclase and magnetite, which yields high Sr/Y. Such magmas might eventually ascend through the crust and reach shallower depths, ultimately exsolving fluids and volatiles necessary to form magmatic-hydrothermal mineral systems. On the other hand, if the same magma undergoes a rapid decompression, plagioclase and magnetite will precede amphibole crystallization, yielding low Sr/Y and less hydrous magmas. In addition, magnetite-induced sulfide saturation will deplete the system in chalcophile elements prior to fluid exsolution, resulting in economically barren magmas. Chiaradia's model adequately explains the low Sr/Y of OMS's group II granitoids, that still show reasonable fO_2 for the formation of porphyry Au – Cu deposits and is compatible with amphibole, more likely on a late stage of the crystallizing sequence. The YMS marks a transition from evolved-arc to post-orogenic or collisional tectonic settings and, with the exception of intermediate V3 volcanics, amphibole is absent in all units, implying in anhydrous magmas with low Sr/Y. However, as mentioned on the previous section, YMS's petrogenesis involves remobilization of subduction-modified mantle and possibly lower crust, which confers this magmatic sequence its metallogenetic potential for gold-rich magmatic-hydrothermal mineral deposits.

6. Conclusions

The relevance of this study regards how the tectonic context translates into metallogenetic potential for base and precious metal occurrences in south-central Amazonian Craton. Results acquired allowed a better understanding on the magmatic evolution and on the tectonic context of the host rocks from selected mineral deposits in the Tapajós Mineral Province (TMP). Discussion and conclusions might be understood as a first step towards a unified metallogenetic model for the magmatic-hydrothermal mineralizations in the TMP. The different mineralizing systems are hosted either by igneous suites of 2.00 – 1.95 Ga, designated as the older magmatic sequence (OMS), or by igneous suites of 1.90 – 1.86 Ga, treated as the younger magmatic sequence (YMS).

OMS rocks might be divided into three groups. Group i correlate with the Cuiú-Cuiú Complex and comprises peraluminous granites and granodiorites that represent the first batches of arc-magmatism on the TMP (granodiorite sample dated at 2011 Ma), which is characterized by a strong crustal component and an oxidizing and dry petrologic evolution. The $X^{melt}_{Ce^{4+}}/X^{melt}_{Ce^{3+}}$ zircon-based oxy-barometer indicate fO_2 values close to or slightly below the FMQ buffer ($-2 \leq \Delta FMQ \leq 0$). However, due to its anhydrous trend these rocks show a low favorability for the formation of magmatic-hydrothermal mineral systems.

Group II rocks are common and widespread in the TMP, correspond to the Creporizão Intrusive Suite, comprises metaluminous to peraluminous granites (s.l) that evolved on an amphibole and magnetite bearing trend, and represents the evolution of the arc-magmatism. The granodioritic porphyry dated at 1986 Ma represents this stage, which is characterized by the lowest magmatic temperature 768 °C. fO_2 constraints corroborate the more oxidized trend for these rocks ($0 \leq \Delta FMQ \leq +4$), rendering their potential fertility for the formation of porphyry Cu – Au mineralizations. The low Sr/Y ratio reflects a rapid decompression, enabling plagioclase fractionation prior to amphibole extraction in spite of hydrous magmas. On the field, group II rocks are commonly affected by hydrothermal alteration, with disseminated gold or gold and chalcopyrite bearing veins and veinlets most commonly found on the sericitic zone, with potassic and propylitic alterations also economically relevant and barren sodic and argilic alterations.

Group III comprises lower silica, high-K, metaluminous, ferroan, reduced and anhydrous syenites and monzonites of 1993 and 1974 Ma, generated through decompression melting of metasomatized mantle, which yields high magmatic temperatures (TZirc.Ti from 786 to 811 °C). These rocks are rarer and have only been reported in the Patrocínio and Coringa deposits (southern TMP) on drill core sampling. fO_2 between $\Delta FMQ = -1$ and $+1$ positions these rocks on an intermediate redox state within OMS, which contrasts with its ilmenite-bearing evolution. Such geochemistry attributes are understood as diagnostic of an interaction between groups II and III melts, which adequately explains the magmatic fO_2 estimates. By itself, group III should not be considered economically fertile, nevertheless, the group's metallogenetic potential lies exactly on its interaction with the coeval, more hydrous and oxidizing group II melts. The end products are represented by syenites and monzonites affected by sericitic, chloritic and carbonate alterations with disseminated pyrrhotite-pyrite ± gold with less frequent gold bearing pyrite veinlets.

YMS comprises rocks from the Parauari Intrusive Suite and from the Iriri Group, and is represented in the Batalha, Palito, São Jorge and V3 deposits. Field relationships between the older and younger sequences are rare, but Iriri volcanics are found as dykes within OMS granitoids or define lava-flows, whereas the intrusive units define round-shaped plutons. Whereas intermediate V3 volcanics share similar geochemical features with the OMS, acid V3 and the Batalha and Palito granitoids are essentially ferroan and evolved on a magnetite- and amphibole-free trend, suggesting anhydrous and reduced parental magmas. We interpret such differences as symptomatic of a changing tectonic framework within the TMP, from magmatic-arc (OMS) to a post-orogenic or collisional setting. As subduction stalls (or upon the progressive flattening of the slab) magmatism gets dryer, comparatively reduced and, in theory, less favorable for the formation of magmatic-hydrothermal mineral deposits. However, YMS' metallogenetic potential is related with

remobilization or melting of SCLM and/or lower crustal, gold-rich sulfides formed on the previous magmatic events. The outcome is identified in the Batalha and Palito deposits, with disseminated gold and gold bearing sulfide veinlets preferentially distributed in the sericitic zone, and in the V3 mineralization, with alunite and gold bearing sulfide veinlets hosted by hydrothermal breccias on the advanced argilic alteration. Therefore, YMS should be treated as metallogenetic fertile for the formation of gold-rich magmatic-hydrothermal systems, since it efficiently mobilizes previously formed sulfides.

Declaration of Competing Interest

The authors declare that they have no known competing financial interests or personal relationships that could have appeared to influence the work reported in this paper.

Acknowledgements

The results presented in this research were funded by the National Council for Scientific and Technological Development (CNPq) through the processes 550342/2011-7 and 573733/2008-2, and by the Society of Economic Geologists (SEG) through its McKinstry fund. The authors are also thankful for the ETH's Department of Earth Sciences for the in-situ zircon analyses. Scholarships for Lucas V. Cassini were provided by the Coordination for the Improvement of Higher Education Personnel (CAPES) and CNPq from Brazil, and by the French agency Campus France through its Eiffel Bourse d'excellence (#P714383D).

Appendix A. Supplementary data

Supplementary data to this article can be found online at https://doi.org/10.1016/j.oregeorev.2021.104643.

References

Annen, C., Blundy, J.D., Sparks, R.S.J., 2006. The genesis of intermediate and silicic magmas in deep crustal hot zones. J. Petrol. 47, 505–539. https://doi.org/10.1093/petrology/egi084.

Bachmann, O., Dungan, M.A., Bussy, F., 2005. Insights into shallow magmatic processes in large silicic magma bodies: the trace element record in the Fish Canyon magma body, Colorado. Contribut. Mineral. Petrol. 149 (3), 338–349. https://doi.org/10.1007/s00410-005-0653-z.

Ballard, J.R., Palin, J.M., Campbell, I.H., 2002. Relative oxidation states of magmas inferred from Ce(IV)/ Ce(III) in zircon : application to porphyry copper deposits of northern Chile. Contrib. Miner. Petrol. 347–364 https://doi.org/10.1007/s00410-002-0402-5.

Bell, E.A., Boehnke, P., Barboni, M., Harrison, T.M., 2019. Tracking chemical alteration in magmatic zircon using rare earth element abundances. Chem. Geol. 510, 56–71. https://doi.org/10.1016/j.chemgeo.2019.02.027.

Bell, E.A., Boehnke, P., Harrison, T.M., 2016. Recovering the primary geochemistry of Jack Hills zircons through quantitative estimates of chemical alteration. Geochim. Cosmochim. Acta 191, 187–202. https://doi.org/10.1016/j.gca.2016.07.016.

Biondi, J.C., Borgo, A., Chauvet, A., Monié, P., Bruguier, O., Ocampo, R., 2018. Structural, mineralogical, geochemical and geochronological constraints on ore genesis of the gold-only Tocantinzinho deposit (Para State, Brazil). Ore Geol. Rev. 102, 154–194. https://doi.org/10.1016/j.oregeorev.2018.08.007.

Blundy, J., Wood, B., 1994. Prediction of crystal–melt partition coefficients from elastic moduli. Nature 372 (6505), 452–454. https://doi.org/10.1038/372452a0.

Bogaerts, M., Scaillet, B., Auwera, J.V., 2006. Phase equilibria of the Lyngdal granodiorite (Norway): Implications for the origin of metaluminous ferroan granitoids. J. Petrol. 47, 2405–2431. https://doi.org/10.1093/petrology/egl049.

Bonin, B., 2004. Do coeval mafic and felsic magmas in post-collisional to within-plate regimes necessarily imply two contrasting, mantle and crustal, sources? A review. Lithos 78 (1-2), 1–24.

Bonin, B., 1990. From orogenic to anorogenic settings: evolution of granitoid suites after a major orogenesis. Geol. J. 25 (3-4), 261–270. https://doi.org/10.1002/gj.3350250309.

Bonin, B., Janoušek, V., Moyen, J.-F., 2020. Chemical variation, modal composition and classification of granitoids. Geol. Soc. Lond. Spec. Publ. 491 (1), 9–51.

Borges, R.M.K., Dall'Agnol, R., Lamarão, C.N., Figueiredo, M.A.B.M., Leite, A.A.d.S., Barros, C.E.d.M., Costi, H.T., 2009. Petrografia, química mineral e processos hidrotermais associados ao depósito de ouro São Jorge, Província Aurífera do Tapajós, Cráton Amazônico. Rev. Brasil. Geoci. 39 (2), 375–393.

Borgo, A., Biondi, J.C., Chauvet, A., Bruguier, O., Monié, P., Baker, T., Ocampo, R., Friedman, R., Mortensen, J., 2017. Geochronological, geochemical and petrographic constraints on the Paleoproterozoic Tocantinzinho gold deposit (Tapajos Gold Province, Amazonian Craton - Brazil): Implications for timing, regional evolution and deformation style of its host rocks. J. S. Am. Earth Sci. 75, 92–115. https://doi.org/10.1016/j.jsames.2017.02.003.

Bouilhol, P., Magni, V., van Hunen, J., Kaislaniemi, L., 2015. A numerical approach to melting in warm subduction zones. Earth Planet. Sci. Lett. 411, 37–44. https://doi.org/10.1016/j.epsl.2014.11.043.

Boynton, W.V., 1984. Geochemistry of the rare earth elements: meteorite studies. In: Henderson P. (ed.), Rare earth element geochemistry. Elsevier, pp. 63-114. pp. 63–114.

Carneiro, C.d.C., Juliani, C., Carreiro-Araujo, S.A., Monteiro, L.V.S., Crosta, A.P., Fernandes, C.M.D., 2019. New crustal framework in the amazon craton based on geophysical data: evidences of deep east-west trending suture zones. IEEE Geosci. Remote Sens. Lett. 16 (1), 20–24. https://doi.org/10.1109/LGRS.2018.2867551.

Cassini, L.V., 2016. Alteração Hidrotermal e Gênese da Mineralização Aurífera do Patrocínio, Província Mineral do Tapajós (PA). University of São Paulo, Brazil, p. 151 pp.. Unpublished M.Sc thesis.

Cassini, L.V., Moyen, J.-F., Juliani, C., 2020. Orosirian magmatism in the tapajós mineral province (amazonian craton): the missing link to understand the onset of paleoproterozoic tectonics. Lithos 356-357, 105350. https://doi.org/10.1016/j.lithos.2019.105350.

Chappell, B.W., White, A.J.R., 2001. Two contrasting granite types: 25 years later. Aust. J. Earth Sci. 48 (4), 489–499. https://doi.org/10.1046/j.1440-0952.2001.00882.x.

Chelle-Michou, C., Chiaradia, M., Ovtcharova, M., Ulianov, A., Wotzlaw, J.F., 2014. Zircon petrochronology reveals the temporal link between porphyry systems and the magmatic evolution of their hidden plutonic roots (the Eocene Coroccohuayco deposit, Peru). Lithos 198–199, 129–140. https://doi.org/10.1016/j.lithos.2014.03.017.

Chelle-Michou, C., Rottier, B., Caricchi, L., Simpson, G., 2017. Tempo of magma degassing and the genesis of porphyry copper deposits. Nat. Publish. Group 7 (1). https://doi.org/10.1038/srep40566.

Chen, J.L., Xu, J.F., Wang, B.D., Yang, Z.M., Ren, J.B., Yu, H.X., Liu, H., Feng, Y., 2015. Geochemical differences between subduction- and collision-related copper-bearing porphyries and implications for metallogenesis. Ore Geol. Rev. 70, 424–437. https://doi.org/10.1016/j.oregeorev.2015.01.011.

Chiaradia, M., Ulianov, A., Kouzmanov, K., Beate, B., 2012. Why large porphyry Cu deposits like high Sr/Y magmas? Sci. Rep. 2 (1) https://doi.org/10.1038/srep00685.

Clemens, J.D., Stevens, G., 2012. What controls chemical variation in granitic magmas? Lithos 134–135, 317–329. https://doi.org/10.1016/j.lithos.2012.01.001.

Clemens, J.D., Stevens, G., Farina, F., 2011. The enigmatic sources of I-type granites: the peritectic connexion. Lithos 126 (3-4), 174–181. https://doi.org/10.1016/j.lithos.2011.07.004.

Cloos, M., Sapiie, B., Quarles van Ufford, A., Weiland, R.J., Warren, P.Q., McMahon, T.P., 2005. In: Collisional Delamination in New Guinea: The Geotectonics of Subducting Slab Breakoff. Geological Society of America. https://doi.org/10.1130/2005.2400.

Cooke, D.R., Hollings, P., Wilkinson, J.J., Tosdal, R.M., 2014. Geochemistry of Porphyry Deposits. In: Treatise on Geochemistry. Elsevier, pp. 357–381. https://doi.org/10.1016/B978-0-08-095975-7.01116-5.

Dall'Agnol, R., Rämö, O.T., de Magalhães, M.S., Macambira, M.J.B., 1999. Petrology of the anorogenic, oxidised Jamon and Musa granites, Amazonian Craton: implications for the genesis of Proterozoic A-type granites. Lithos 46 (3), 431–462. https://doi.org/10.1016/S0024-4937(98)00077-2.

De la Roche, H., Leterrier, J., Grandclaude, P., Marchal, M., 1980. A classification of volcanic and plutonic rocks using R1R2-diagram and major-element analyses — Its relationships with current nomenclature. Chem. Geol. 29 (1-4), 183–210. https://doi.org/10.1016/0009-2541(80)90020-0.

Echeverri Misas, C.M., 2015. Geologia e Alteração Hidrotermal nas Rochas Vulcânicas e Plutônicas Paleoproterozoicas na Porção Sul da Província Mineral do Tapajós (PA). University of São Paulo, Brazil, p. 285 pp.. Unpublished Ph.D thesis.

Fernandes, C.M.D., Juliani, C., 2019. The tectonic controls on the Paleoproterozoic volcanism and the associated metallogeny in the South Amazonian craton, Brazil: Sr–Nd–Pb isotope constraints. Precambr. Res. 331, 105354. https://doi.org/10.1016/j.precamres.2019.105354.

Fernandes, C.M.D., Juliani, C., Monteiro, L.V.S., Lagler, B., Echeverri Misas, C.M., 2011. High-K calc-alkaline to A-type fissure-controlled volcano-plutonism of the São Félix do Xingu region, Amazonian craton, Brazil: Exclusively crustal sources or only mixed Nd model ages? J. S. Am. Earth Sci. 32 (4), 351–368. https://doi.org/10.1016/j.jsames.2011.03.004.

Ferré, E.C., Caby, R., Peucat, J.J., Capdevila, R., Monié, P., 1998. Pan-African, post-collisional, ferro-potassic granite and quartz-monzonite plutons of Eastern Nigeria. Lithos 45 (1-4), 255–279. https://doi.org/10.1016/S0024-4937(98)00035-8.

Ferreira, V.P., Sial, A.N., Jardim de Sá, E.F., 1998. Geochemical and isotopic signatures of Proterozoic granitoids in terranes of the Borborema structural province, northeastern Brazil. J. S. Am. Earth Sci. 11 (5), 439–455. https://doi.org/10.1016/S0895-9811(98)00027-3.

Ferry, J.M., Watson, E.B., 2007. New thermodynamic models and revised calibrations for the Ti-in-zircon and Zr-in-rutile thermometers. Contrib. Miner. Petrol. 154 (4), 429–437. https://doi.org/10.1007/s00410-007-0201-0.

Frost, B.R., Barnes, C.G., Collins, W.J., Arculus, R.J., Ellis, D.J., Frost, C.D., 2001. A Geochemical Classification for Granitic Rocks 42, 2033–2048.

Frost, C.D., Frost, B.R., 2013. Proterozoic ferroan feldspathic magmatism. Precambr. Res. 228, 151–163. https://doi.org/10.1016/j.precamres.2013.01.016.

Frost, C.D., Frost, B.R., 2011. On Ferroan (A-type) Granitoids : their Compositional Variability and Modes of Origin. J. Petrol. 52, 39–53. https://doi.org/10.1093/petrology/egq070.

Grondahl, C., Zajacz, Z., 2017. Magmatic controls on the genesis of porphyry Cu–Mo–Au deposits: the Bingham Canyon example. Earth Planet. Sci. Lett. 480, 53–65. https://doi.org/10.1016/j.epsl.2017.09.036.

Guimarães, S.B., Klein, E.L., Harris, C., Costa, I.S.L., 2021. Metallogenesis of the orosirian epithermal coringa gold-silver (Cu-Pb-Zn) deposit, southeastern Tapajós mineral Province, Amazonian craton. Brazil. Ore Geology Reviews 128, 103908. https://doi.org/10.1016/j.oregeorev.2020.103908.

Gutiérrez, D.F.G., 2018. Petrogênese e metalogenia do magmatismo Paleoproterozoico na porção sul da Província Mineral do Tapajós, Cráton Amazônico. University of São Paulo, Brazil, p. 234 pp.. Unpublished Ph.D thesis.

Harrison, T.M., Watson, E.B., Aikman, A.B., 2007. Temperature spectra of zircon crystallization in plutonic rocks. Geology 35 (7), 635. https://doi.org/10.1130/G23505A.1.

Holliday, J., Wilson, A., Blevin, P., Tedder, I., Dunham, P., Pfitzner, M., 2002. Porphyry gold-copper mineralisation in the Cadia district, Eastern Lachlan Fold Belt, New South Wales, and its relationship to shoshonitic magmatism. Miner. Depos. 37 (1), 100–116. https://doi.org/10.1007/s00126-001-0233-8.

Hou, Z., Zheng, Y., Yang, Z., Rui, Z., Zhao, Z., Jiang, S., Qu, X., Sun, Q., 2013. Contribution of mantle components within juvenile lower-crust to collisional zone porphyry Cu systems in Tibet. Miner. Depos. 48 (2), 173–192. https://doi.org/10.1007/s00126-012-0415-6.

Huston, D.L., Morant, P., Pirajno, F., Cummins, B., Baker, D., Mernagh, T.P., 2007. Chapter 4.4 Paleoarchean Mineral Deposits of the Pilbara Craton: Genesis, Tectonic Environment and Comparisons with Younger Deposits. Developments in Precambrian Geology 15, 411–450. doi:10.1016/S0166-2635(07)15044-1.

Janoušek, V., Farrow, C.M., Erban, V., 2006. Interpretation of whole-rock geochemical data in igneous geochemistry: Introducing Geochemical Data Toolkit (GCDkit). J. Petrol. 47, 1255–1259. https://doi.org/10.1093/petrology/egl013.

Janoušek, V., Moyen, J.-F., Martin, H., Erban, V., Farrow, C., 2016. In: Geochemical Modelling of Igneous Processes – Principles And Recipes in R Language. Springer Berlin Heidelberg, Berlin, Heidelberg, pp. 69–80. https://doi.org/10.1007/978-3-662-46792-3_6.

Juliani, C., Corrêa-Silva, R.H., Monteiro, L.V.S., Bettencourt, J.S., Nunes, C.M.D., 2002. The Batalha Au-granite system-Tapajós Gold Province, Amazonian craton, Brazil : hydrothermal alteration and regional implications. Precambr. Res. 119, 225–256.

Juliani, C., Rye, R.O., Nunes, C.M.D., Snee, L.W., Corrêa Silva, R.H., Monteiro, L.V.S., Bettencourt, J.S., Neumann, R., Neto, A.A., 2005. Paleoproterozoic high-sulfidation mineralization in the Tapajós gold province, Amazonian Craton, Brazil: geology, mineralogy, alunite argon age, and stable-isotope constraints. Chem. Geol. 215 (1-4), 95–125. https://doi.org/10.1016/j.chemgeo.2004.06.035.

Klein, E.L., Almeida, M.E., Vasquez, M.L., Bahia, R.B.C., Quadros, M.L. do E.S., Ferreira, A.L., 2001. Geologia e recursos minerais da Província Mineral do Tapajós. Folhas SB.21-V-D, SB.21-Y-B, SB.21-X-C e SB.21-Z-C. Estados do Pará e Amazonas. Companhia de Pesquisa de Recursos-CRPM, Brasília, Brazil, p. 100 (in portuguese).

Kouankap Nono, G.D., Nzenti, J.P., Suh, C.E., Ganno, S., 2010. Geochemistry of ferriferous, high-K Calc-alkaline granitoids from the banefo-mvoutsaha massif (NE Bafoussam), central domain of the pan- african fold belt, cameroon~!2009-11-12~! 2010-01-05~!2010-03-11~! Open Geol. J. 4 (1), 15–28. https://doi.org/10.2174/1874262901004010015.

Lamarão, C.N., Dall'Agnol, R., Lafon, J.-M., Lima, E.F., 2002. Geology, geochemistry, and Pb-Pb zircon geochronology of the Paleoproterozoic magmatism of Vila Riozinho, Tapajós Gold Province, Amazonian craton, Brazil. Precambr. Res. 119 (1-4), 189–223.

Lamarão, C.N., Dall'Agnol, R., Pimentel, M.M., 2005. Nd isotopic composition of Paleoproterozoic volcanic and granitoid rocks of Vila Riozinho: implications for the crustal evolution of the Tapajós gold province, Amazon craton. J. S. Am. Earth Sci. 18 (3-4), 277–292. https://doi.org/10.1016/j.jsames.2004.11.005.

Large, S.J.E., von Quadt, A., Wotzlaw, J.-F., Guillong, M., Heinrich, C.A., 2018. Magma evolution leading to porphyry Au-Cu mineralization at the ok tedi deposit, Papua New Guinea: trace element geochemistry and high-precision geochronology of igneous zircon. Econ. Geol. 113, 39–61. https://doi.org/10.5382/econgeo.2018.4543.

Laurent, O., Rapopo, M., Stevens, G., Moyen, J.-F., Martin, H., Doucelance, R., Bosq, C., 2014. Contrasting petrogenesis of Mg–K and Fe–K granitoids and implications for post-collisional magmatism: Case study from the Late-Archean Matok pluton (Pietersburg block, South Africa). Lithos 196–197, 131–149. https://doi.org/10.1016/J.LITHOS.2014.03.006.

Lee, R.G., Byrne, K., D'Angelo, M., Hart, C.J.R., Hollings, P., Gleeson, S.A., Alfaro, M., 2021. Using zircon trace element composition to assess porphyry copper potential of the Guichon Creek batholith and Highland Valley Copper deposit, south-central British Columbia. Miner Depos. 56 (2), 215–238.

Liégeois, J.-P., Navez, J., Hertogen, J., Black, R., 1998. Contrasting origin of post-collisional high-K calc-alkaline and shoshonitic versus alkaline and peralkaline granitoids. The use of sliding normalization. Lithos 45 (1-4), 1–28.

Loader, M.A., Wilkinson, J.J., Armstrong, R.N., 2017. The effect of titanite crystallisation on Eu and Ce anomalies in zircon and its implications for the assessment of porphyry Cu deposit fertility. Earth Planet. Sci. Lett. 472, 107–119. https://doi.org/10.1016/j.epsl.2017.05.010.

Lopes, A.A.C., Moura, M.A., 2019. The tocantinzinho paleoproterozoic porphyry-style gold deposit, tapajós mineral province (Brazil): geology, petrology and fluid inclusion evidence for ore-forming processes. Minerals 9, 29. https://doi.org/10.3390/min9010029.

Loucks, R.R., 2014. Distinctive composition of copper-ore-forming arc magmas. Aust. J. Earth Sci. 61 (1), 5–16. https://doi.org/10.1080/08120099.2013.865676.

Moyen, J.-F., 2009. High Sr/Y and La/Yb ratios: the meaning of the "adakitic signature". Lithos 112 (3-4), 556–574. https://doi.org/10.1016/j.lithos.2009.04.001.

Moyen, J.-F., Laurent, O., Chelle-Michou, C., Couzinié, S., Vanderhaeghe, O., Zeh, A., Villaros, A., Gardien, V., 2017. Collision vs. subduction-related magmatism: two contrasting ways of granite formation and implications for crustal growth. Lithos 277, 154–177. https://doi.org/10.1016/j.lithos.2016.09.018.

Mungall, J.E., 2002. Roasting the mantle: Slab melting and the genesis of major Au and Au-rich Cu deposits. Geology 30, 915–918. https://doi.org/10.1130/0091-7613(2002)030<0915:RTMSMA>2.0.CO;2.

Ohta, T., Arai, H., 2007. Statistical empirical index of chemical weathering in igneous rocks: A new tool for evaluating the degree of weathering. Chem. Geol. 240 (3-4), 280–297. https://doi.org/10.1016/j.chemgeo.2007.02.017.

Paton, C., Hellstrom, J., Paul, B., Woodhead, J., Hergt, J., 2011. Iolite: Freeware for the visualisation and processing of mass spectrometric data. J. Anal. At. Spectrom. 26, 2508–2518. https://doi.org/10.1039/c1ja10172b.

Pirajno, F., 2009. In: Hydrothermal Processes and Mineral Systems. Springer Netherlands, Dordrecht, pp. 355–533. https://doi.org/10.1007/978-1-4020-8613-7_5.

Richards, J.P., 2015a. The oxidation state, and sulfur and Cu contents of arc magmas: implications for metallogeny. Lithos 233, 27–45. https://doi.org/10.1016/j.lithos.2014.12.011.

Richards, J.P., 2015b. Tectonic, magmatic, and metallogenic evolution of the Tethyan orogen: From subduction to collision. Ore Geol. Rev. 70, 323–345. https://doi.org/10.1016/j.oregeorev.2014.11.009.

Richards, J.P., 2014. Porphyry and Related Deposits in Subduction and Post-Subduction Settings. Acta Geol. Sin. 88 (s2), 535–537.

Richards, J.P., 2011a. Magmatic to hydrothermal metal fluxes in convergent and collided margins. Ore Geol. Rev. 40 (1), 1–26. https://doi.org/10.1016/j.oregeorev.2011.05.006.

Richards, J.P., 2011b. High Sr/Y arc magmas and porphyry Cu ± Mo ± Au deposits: Just add water. Econ. Geol. 106, 1075–1081. https://doi.org/10.2113/econgeo.106.7.1075.

Richards, J.P., 2009. Postsubduction porphyry Cu-Au and epithermal Au deposits: products of remelting of subduction-modified lithosphere. Geology 37, 247–250. https://doi.org/10.1130/G25451A.1.

Rollinson, H.R., 1993. Using geochemical data : evaluation, presentation, interpretation. Longman Scientific & Technical.

Santos, J.O.S., Groves, D.I., Hartmann, L.A., Moura, M.A., McNaughton, N.J., 2001. Gold deposits of the tapajós and alta floresta domains, tapajós-parima orogenic belt, Amazon Craton, Brazil. Miner. Depos. 36 (3-4), 278–299. https://doi.org/10.1007/s001260100172.

Santos, J.O.S., Hartmann, L.A., Faria, M.S., Riker, S.R., Miguel, M., Almeida, M.E., Mcnaughton, N.J., 2006. A compartimentação do Cráton Amazonas em províncias: avanços ocorridos no periodo 2000–2006. The Ninth Simpósio de Geologia da Amazônia, Belém, Brazil (in portuguese), p. 4.

Santos, J.O.S., Hartmann, L.A., Gaudette, H.E., Groves, D.I., Mcnaughton, N.J., Fletcher, I.R., 2000. A new understanding of the provinces of the Amazon craton based on integration of field mapping and U-Pb and Sm-Nd geochronology. Gondwana Res. 3 (4), 453–488. https://doi.org/10.1016/S1342-937X(05)70755-3.

Santos, J.O.S., Hartmann, L.A., McNaughton, N.J., Fletcher, I.R., 2002. Timing of mafic magmatism in the Tapajós Province (Brazil) and implications for the evolution of the Amazon Craton: evidence from baddeleyite and zircon U-Pb SHRIMP geochronology. J. S. Am. Earth Sci. 15 (4), 409–429. https://doi.org/10.1016/S0895-9811(02)00061-5.

Santos, J.O.S., Van Breemen, O.B., Groves, D.I., Hartmann, L.A., Almeida, M.E., McNaughton, N.J., Fletcher, I.R., 2004. Timing and evolution of multiple Paleoproterozoic magmatic arcs in the Tapajós Domain, Amazon Craton: Constraints from SHRIMP and TIMS zircon, baddeleyite and titanite U-Pb geochronology. Precambr. Res. 131 (1-2), 73–109. https://doi.org/10.1016/j.precamres.2004.01.002.

Shand, S.J., 1943. Eruptive Rocks, 2nd edn. New York: John Wiley, 444 pp. Geological Magazine. doi:10.1017/S0016756800075026.

Sillitoe, R.H., 2010. Porphyry copper systems. Econ. Geol. 105 (1), 3–41.

Sinclair, W.D., 2007. Porphyry Deposits. In: Mineral Deposits of Canada: A Synthesis of Major Deposit-Types, District Metallogeny, the Evolution of Geological Provinces, and Exploration Methods. Geological Association of Canada, Mineral Deposits Division, pp. 223–243.

Smythe, D.J., Brenan, J.M., 2016. Magmatic oxygen fugacity estimated using zircon-melt partitioning of cerium. Earth Planet. Sci. Lett. 453, 260–266. https://doi.org/10.1016/j.epsl.2016.08.013.

Sobolev, A.V., Chaussidon, M., 1996. H2O concentrations in primary melts from supra-subduction zones and mid-ocean ridges: Implications for H2O storage and recycling in the mantle. Water 137 (1-4), 45–55.

Stein, H.J., Hannah, J.L., Zimmerman, A., Markey, R.J., Sarkar, S.C., Pal, A.B., 2004. A 2.5 Ga porphyry Cu-Mo-Au deposit at Malanjkhand, central India: Implications for Late Archean continental assembly. Precambr. Res. 134 (3-4), 189–226. https://doi.org/10.1016/j.precamres.2004.05.012.

Sun, S., McDonough, W.F., 1989. Chemical and isotopic systematics of oceanic basalts: implications for mantle composition and processes. Geol. Soc. Lond. Spec. Publ. 42, 313–345. https://doi.org/10.1144/GSL.SP.1989.042.01.19.

Sun, W., Huang, R.-F., Li, H.e., Hu, Y.-B., Zhang, C.-C., Sun, S.-J., Zhang, L.-P., Ding, X., Li, C.-Y., Zartman, R.E., Ling, M.-X., 2015. Porphyry deposits and oxidized magmas. Ore Geol. Rev. 65, 97–131. https://doi.org/10.1016/j.oregeorev.2014.09.004.

Tassinari, C.C.G., Macambira, M.J.B., 1999. Geochronological provinces of the Amazonian Craton. Episodes 22, 174–182. https://doi.org/10.1080/00206819709465329.

Tokashiki, C. do C., 2015. Mineralizações Low- e Intermediate Sulfidation de Ouro e de Metais de Base em Domos de Riolito Paleoproterozócios na Porção Sul da Provincia

Mineral do Tapajós. Unpublished Ph.D thesis, University of São Paulo, Brazil, 188 pp.
Trail, D., Bruce Watson, E., Tailby, N.D., 2012. Ce and Eu anomalies in zircon as proxies for the oxidation state of magmas. Geochim. Cosmochim. Acta 97, 70–87. https://doi.org/10.1016/j.gca.2012.08.032.
Vander Auwera, J., Bolle, O., Bingen, B., Liégeois, J.-P., Bogaerts, M., Duchesne, J.C., De Waele, B., Longhi, J., 2011. Sveconorwegian massif-type anorthosites and related granitoids result from post-collisional melting of a continental arc root. Earth Sci. Rev. 107 (3-4), 375–397. https://doi.org/10.1016/j.earscirev.2011.04.005.
Vermeesch, P., 2018. IsoplotR: A free and open toolbox for geochronology. Geosci. Front. 9 (5), 1479–1493. https://doi.org/10.1016/j.gsf.2018.04.001.
Villas, R.N.N., Santiago, É.S.B., Castilho, M.P., 2013. Contexto geológico, estudos isotópicos (C, O e Pb) e associação metálica do depósito aurífero Tocantinzinho, domínio Tapajós, Província Tapajós-Parima. Geol. USP - Série Científica 13 (1), 119–138. https://doi.org/10.5327/Z1519-874X2013000100008.
Villaseca, C., Barbero, L., Herreros, V., 1998. A re-examination of the typology of peraluminous granite types in intracontinental orogenic belts. Trans. R. Soc. Edinburgh Earth Sci. 89 (2), 113–119.
Virgo, D., Mysen, B.O., Kushiro, I., 1980. Anionic constitution of 1-atmosphere silicate melts: implications for the structure of igneous melts. Science 208 (4450), 1371–1373.
Wang, R., Weinberg, R.F., Collins, W.J., Richards, J.P., Zhu, D., cheng, 2018. Origin of postcollisional magmas and formation of porphyry Cu deposits in southern Tibet. Earth Sci. Rev. 181, 122–143. https://doi.org/10.1016/j.earscirev.2018.02.019.
Waters, L.E., Lange, R.A., 2015. An updated calibration of the plagioclase-liquid hygrometer-thermometer applicable to basalts through rhyolites. Am. Mineral. 100 (10), 2172–2184. https://doi.org/10.2138/am-2015-5232.
Watson, E.B., Harrison, T.M., 1983. Zircon saturation revisited: temperature and composition effects in a variety of crustal magma types. Earth Planet. Sci. Lett. 64 (2), 295–304. https://doi.org/10.1016/0012-821X(83)90211-X.
Zhang, D., Audétat, A., 2017. What caused the formation of the giant bingham canyon Porphyry Cu-Mo-Au deposit? Insights from melt inclusions and magmatic sulfides. Econ. Geol. 112 (2), 221–244. https://doi.org/10.2113/econgeo.112.2.221.
Zou, X.Y., Qin, K.Z., Han, X.L., Li, G.M., Evans, N.J., Li, Z.Z., Yang, W., 2019. Insight into zircon REE oxy-barometers: A lattice strain model perspective. Earth Planet. Sci. Lett. 506, 87–96. https://doi.org/10.1016/j.epsl.2018.10.031.